

Energy-efficient flow control via optimized synthetic jet placement using deep reinforcement learning*

Wang Jia and Hang Xu[†]

School of Ocean and Civil Engineering, Shanghai Jiao Tong University, Shanghai, 200240, China

(Dated: December 11, 2024)

This study utilizes deep reinforcement learning (DRL) to develop flow control strategies for circular and square cylinders, enhancing energy efficiency and minimizing energy consumption while addressing the limitations of traditional methods. We find that the optimal jet placement for both square and circular cylinders is at the main flow separation point, achieving the best balance between energy efficiency and control effectiveness. For the circular cylinder, positioning the jet at approximately 105° from the stagnation point requires only 1% of the inlet flow rate and achieves an 8% reduction in drag, with energy consumption one-third of that at other positions. For the square cylinder, placing the jet near the rear corner requires only 2% of the inlet flow rate, achieving a maximum drag reduction of 14.4%, whereas energy consumption near the front corner is 27 times higher, resulting in only 12% drag reduction. In multi-action control, the convergence speed and stability are lower compared to single-action control, but activating multiple jets significantly reduces initial energy consumption and improves energy efficiency. Physically, the interaction of the synthetic jet with the flow generates new vortices that modify the local flow structure, significantly enhancing the cylinder's aerodynamic performance. Our control strategy achieves a superior balance between energy efficiency and control performance compared to previous studies, underscoring its significant potential to advance sustainable and effective flow control.

I. INTRODUCTION

Active flow control (AFC) involves regulating and controlling fluid flow through external mechanisms such as injection, suction, or vibration to optimize flow characteristics and enhance system efficiency, performance, and stability. Despite significant advancements in this field over the past few decades, there remain unresolved challenges, particularly in addressing the nonlinear complexities inherent in fluid dynamics [1]. Fluid dynamics problems are intrinsically nonlinear, especially when dealing with turbulent and separated flows, where the flow behavior is extremely complex and difficult to control accurately using traditional analytical or numerical methods [2]. The challenges are further compounded in high-dimensional and multi-scale problems, where finding a global optimum solution is particularly challenging. Consequently, there are still numerous difficulties in optimizing control strategies, achieving real-time control, enhancing system robustness, and reducing energy consumption [3]. Addressing these issues will not only help overcome existing technical barriers but also promote the application and development of AFC technologies in a broader range of fields [4].

The rapid development of artificial intelligence brings new vitality to the field of flow control, with reinforcement learning (RL) emerging as a key machine learning algorithm that effectively addresses complex decision-making and control problems [5, 6]. The core mechanism of RL lies in the agent's capability to interact with the environment, gradually optimizing its strategy based on rewards or penalties received from its actions, with the goal of maximizing cumulative rewards [7]. Reinforcement learning agents possess the ability for long-term planning and decision-making, continuously adjusting their behavior strategies in response to environmental feedback, making it a powerful tool for autonomous learning and decision-making [8]. Deep learning (DL) has strong expressive capabilities, allowing it to approximate complex nonlinear functions [9]. When RL is combined with DL to form deep reinforcement learning (DRL), this approach leverages the feature extraction capabilities of DL and the strategy optimization strengths of RL [10]. Consequently, DRL is highly effective at tackling control challenges in high-dimensional, complex state spaces, establishing itself as a powerful technique for advancing flow control technologies and addressing intricate fluid dynamics problems.

The development of DRL traces back to the mid-20th century, with significant progress occurring as deep learning and computational power advance [7]. A pivotal milestone comes in 2013 when Google DeepMind introduces the Deep Q-Network (DQN), demonstrating DRL's remarkable potential in mastering Atari games and establishing it as a prominent and rapidly expanding research area [11]. Subsequent advancements, particularly in proximal policy optimization (PPO) and distributed DRL techniques, further propel the field. PPO addresses the inherent instability of traditional policy gradient methods by introducing a clipped objective function, ensuring stable and efficient policy updates [12]. Distributed DRL, enabling parallel training across multiple machines, greatly improves computational efficiency and scalability [13, 14]. These developments lead to DRL applications in various domains, including AlphaGo's performance in Go, autonomous vehicle navigation, robotic operations,

* Present address: School of Ocean and Civil Engineering, Shanghai Jiao Tong University, Shanghai, 200240, China

[†] hangxu@sjtu.edu.cn

financial trading strategies, and smart manufacturing and healthcare [15, 16]. These applications showcase DRL’s exceptional abilities in high-dimensional perception, continuous decision-making, and complex environment handling, highlighting its immense potential and broad impact in practical applications.

Given the exceptional decision-making capabilities of reinforcement learning, its methods and derivative technologies are seeing widespread development in fluid mechanics, covering various areas such as turbulence modeling, flow prediction, shape optimization, and flow control [17–19]. In the domain of turbulence modeling, [Novati et al.](#) leveraged multi-agent reinforcement learning to automate the discovery of turbulence models [20], while [Kurz et al.](#) utilized a multi-agent reinforcement learning framework to identify the optimal eddy viscosity model for implicitly filtered large eddy simulations [21]. In the field of shape optimization, [Viquerat et al.](#) spearheaded the application of DRL for direct shape optimization, demonstrating that artificial neural networks (ANN) could autonomously generate optimal shapes within a constrained time frame and without prior knowledge, given an appropriate reward mechanism [22]. In the context of flow control, [Rabault et al.](#) introduced the first application of an ANN trained via DRL for flow control, successfully reducing drag by 8% [23]. These studies highlight the significant potential and promising prospects of DRL in the field of fluid mechanics.

AFC techniques that couple CFD with DRL have been extensively studied across various domains, including robustness across Reynolds number (Re), large-scale flow separation control, parallelization strategies, algorithm comparisons, and optimization of probe distributions. Firstly, DRL controllers have shown strong generalization across various Re . [Tang et al.](#) achieved significant drag and lift reductions in cylinder flows [24], while [Wang and Xu](#) demonstrated the DRL agent’s ability to fully suppress vortex shedding across multiple Reynolds numbers [25]. [Ren et al.](#), [Wang et al.](#) further explored DRL in higher Re and 3D flows [26, 27]. Secondly, DRL algorithms have been successfully applied to control complex flow separation phenomena across various configurations, including fluidic pinball systems [28], square cylinders [25], airfoils [29], elliptical cylinders [30], and flat plates [30], showcasing their versatility and robustness. Thirdly, significant advancements have been achieved in refining DRL algorithms and optimizing probe placements, as highlighted by [Li and Zhang](#), [Xia et al.](#), [Suárez et al.](#), [Paris et al.](#) Additionally, parallelization has proven critical for enhancing the efficiency of DRL-based flow control, with studies such as [Rabault and Kuhnle](#), [Wang and Xu](#), [Wang et al.](#) demonstrating its potential to accelerate training and strategy discovery [35–37].

Despite prior studies exploring DRL-based AFC from various perspectives, research in the field of synthetic jet technology has identified that the placement of jet actuators plays a crucial role in determining control effectiveness and energy consumption [38, 39]. The strategic layout of synthetic jets plays a pivotal role in determining their interaction with boundary layer flows, thereby influencing both control performance and energy efficiency [40–42]. As a highly effective flow control method, the optimal positioning of synthetic jets directly dictates their interaction with the boundary layer and the main flow, affecting aerodynamic properties such as drag reduction and lift modulation [42–44]. Moreover, different jet locations lead to varying levels of energy utilization efficiency, where improper placement may result in increased energy consumption with limited control benefits [45, 46]. Thus, investigating the coupling between synthetic jet placement and flow control performance is crucial for uncovering key physical mechanisms and providing theoretical foundations and design principles for achieving energy-efficient flow control. However, a systematic evaluation of the relationship between synthetic jet placement and control performance, particularly in balancing effectiveness and energy consumption, remains insufficiently explored.

Recent studies have begun to explore the influence of synthetic jet actuator placement on flow control. [Chen et al.](#) demonstrated that placing actuators near the rear corners of a square cylinder at $Re = 100$ improved vortex shedding suppression [47]. At higher Reynolds numbers, [Yan et al.](#) showed that positioning actuators near the front corners enhanced performance at $Re = 500$, 1,000, and 2,000 [48]. These studies highlight the growing interest in the design of synthetic jet actuators. However, two key issues remain: firstly, these studies primarily focus on control effectiveness without providing a detailed analysis of the underlying physical mechanisms. Secondly, their qualitative findings on optimal jet placement vary across different Reynolds numbers, leading to inconsistent results [47, 48]. This has prompted significant interest in our own work, where we explored the impact of synthetic jet location and width on flow control performance at $Re = 100$ and 500, using an entropy-regularized reinforcement learning approach [49]. Despite these advances, there remains a lack of comprehensive research on the sensitivity of synthetic jet placement to flow separation suppression in bluff body flows, as well as a unified, fluid mechanics-based qualitative analysis coupled with statistical, quantitative results.

On the other hand, we note that [Yan et al.](#) highlighted the importance of multiple jet actuators, where configurations with multiple independent actuators demonstrated optimal performance [50]. Thus, we have developed a strong interest in comparing the control performance of multiple synthetic jets operating simultaneously with that of single jets working independently. Firstly, the synergy among multiple jets can induce nonlinear flow behaviors, resulting in control effects that differ significantly from those achieved by a single actuator. Evaluating these performance differences can reveal the potential and limitations of synthetic jets in flow control. Secondly, as the number of actuators increases, the interactions between jets and the complexity of energy distribution also rise, potentially impacting energy consumption and control efficiency. A systematic study comparing the control effects of simultaneously activating multiple pairs of synthetic jets versus a single pair not only informs the optimization of jet placement strategies but also provides guidance for achieving efficient and energy-saving flow control.

Given the identified challenges and research gaps in multiple aspects, we conduct a comprehensive analysis of synthetic jet placement to evaluate its impact on flow control performance and energy efficiency. We have designed five synthetic jet placements for cylindrical bodies, resulting in a total of nine jet configuration schemes, including five control strategies for

single synthetic jet actions and four for simultaneous multi-jet actions. Additionally, for square cylinders, we designed four jet placements, leading to seven jet configuration schemes in total, comprising four control strategies for single synthetic jet actions and three for simultaneous multi-jet actions. This approach not only offers a detailed comparison of various actuator placements but also explores the effectiveness of single versus multi-actuator configurations. The innovative contributions of this study are summarized as follows:

- **Sensitivity analysis of synthetic jet placement:** the studies by [Tang et al.](#) and [Rabault et al.](#) have demonstrated the superior decision-making capabilities of deep reinforcement learning in achieving effective flow control. [Tang et al.](#) achieved a 5.7% reduction in drag at $Re = 100$ using two pairs of synthetic jets. In contrast, [Rabault et al.](#), employing the same control algorithm under similar baseline flow conditions, achieved an 8% drag reduction with only one pair of synthetic jets. These findings highlight the significant influence of parameters such as the number and placement of synthetic jet actuators on control performance. Building on previous studies, we posit that the arrangement of synthetic jet placements significantly impacts control performance, making it a critical issue worthy of in-depth investigation. Building on previous studies[23, 24, 50–52], we recognize that the placement of synthetic jets plays a pivotal role in determining control performance, directly influencing the effectiveness and energy efficiency of flow control strategies. A deeper understanding of this relationship is essential not only to optimize actuator configurations but also to establish fundamental principles for designing robust, high-performance control systems applicable across a wide range of flow conditions.
- **Comparison of single-jet and multi-jet control:** [Yan et al.](#) demonstrated in their study of flow around a square cylinder that multiple synthetic jet actuators outperform a single pair, highlighting the potential advantages of multi-jet configurations [50]. However, this conclusion contrasts with findings from studies on circular cylinder flows [23, 24]. To address this discrepancy, our study uniquely compares the performance of single-jet and multi-jet actuation in both square and circular cylinder flow scenarios. By investigating the synergistic effects of multi-jet actuation, we aim to uncover the nonlinear interactions in the flow and evaluate the trade-offs between the two configurations. We provides novel insights into actuator design, particularly in optimizing the balance between control efficiency and energy consumption.
- **Achieving complete suppression of vortex shedding:** previous studies have achieved notable success in drag reduction; however, a common issue persists: the controlled flows in their results still exhibit vortex shedding, leading to oscillations in both lift and drag coefficients, even at $Re = 100$ [23, 24, 34, 53, 54]. This observation prompted us to delve deeper into the underlying mechanisms. Drawing on vortex-induced vibration theory [55], we hypothesize that the residual oscillations in lift and drag coefficients are directly linked to the incomplete suppression of vortex shedding in the controlled flow. We address this challenge by implementing a DRL-based active flow control strategy capable of completely suppressing vortex shedding. Our results demonstrate a fully stabilized flow field, where vortex shedding is entirely eliminated. This is clearly reflected in the lift and drag coefficients, which no longer exhibit any oscillatory behavior, even under the same conditions where previous studies observed persistent instabilities.
- **Enhancing energy efficiency in flow control:** another significant contribution of this study is the exploration of energy-efficient control strategies. We observe that existing studies fail to comprehensively evaluate the control costs when assessing flow control performance. For active flow control strategies to be feasible, they must not only achieve the desired outcomes but also ensure energy efficiency. This requires the control strategies to optimize flow behavior with minimal energy input, thus preventing excessive energy consumption due to the control measures themselves. By leveraging DRL algorithms to explore energy-efficient control strategies, this study not only ensures stable performance but also guarantees that the control solutions are optimized for minimal energy consumption.

We systematically investigates the impact of synthetic jet placement on flow control performance and energy efficiency, providing a comprehensive analysis of the differences between single-jet and multi-jet configurations. By examining their applicability and variations across different bluff body shapes and flow separation characteristics, this research bridges gaps in the understanding of jet placement sensitivity and the synergistic effects of multiple jets. The findings offer new insights into optimizing flow control strategies, balancing control efficiency with energy consumption, and establishing a solid foundation for the design of future actuators. The structure of this paper is organized as follows: In § II, we introduce the research problem and detail the framework for integrating DRL with AFC, including the specifics of the DRL environment, reward functions, and simulation setup. § III focuses on the DRL training results for circular cylinders, highlighting the optimization of jet placement and control strategies to achieve drag reduction and vortex shedding suppression. Similarly, § IV presents the results for square cylinders, emphasizing the unique flow characteristics and control challenges associated with sharp-edged bluff bodies. In § V, we analyze the physical phenomena underlying the DRL-trained control strategies for both cylinder geometries, offering insights into the flow dynamics and the effects of jet configurations on performance metrics such as drag, lift, and energy efficiency. Finally, § VI summarizes the main findings of this study, discusses the implications for actuator design, and outlines potential directions for future research in DRL-based flow control.

II. METHODOLOGY

DRL algorithms are used to manipulate synthetic jets for active flow control, focusing on the impact of jet positioning on flow performance around square and circular cylinders at $Re = 100$. The fundamental numerical methods, software, and key parameters are outlined in § II A. In § II B, we describe the flow characteristics around a circular cylinder and the arrangement of the synthetic jets, while § II C provides corresponding details for a square cylinder. § II D introduces the core concepts, mathematical models, and distinctions of deep learning and reinforcement learning, with a detailed discussion of the PPO algorithm. Lastly, § II E demonstrates the application of DRL algorithms to address flow control challenges, offering a comprehensive overview of the agent-environment framework and related key concepts.

A. Numerical simulation

The behavior of incompressible viscous fluid flow within the domain $\Omega \subset \mathbb{R}^{nd}$ over the time interval $(0, T)$ is described using the Navier-Stokes equations. These equations govern the evolution of the fluid velocity field $\mathbf{u} = \mathbf{u}(\mathbf{x}, t)$ and pressure field $p = p(\mathbf{x}, t)$, where \mathbf{x} represents the spatial coordinates and t denotes time. The governing equations in their non-dimensional form are expressed as:

$$\frac{\partial \mathbf{u}}{\partial t} + \mathbf{u} \cdot (\nabla \mathbf{u}) = -\nabla p + Re^{-1} \Delta \mathbf{u} \quad \text{in } \Omega \times (0, T), \quad (1a)$$

$$\nabla \cdot \mathbf{u} = 0 \quad \text{in } \Omega \times (0, T), \quad (1b)$$

where the Reynolds number is defined as $Re = \frac{UD}{\nu}$, with U being the upstream inlet velocity, D as the characteristic length (the cylinder diameter for a circular cylinder and the length of one side for a square cylinder), and ν denoting the kinematic viscosity of the fluid.

The OpenFOAM, a widely used and flexible Navier-Stokes solver that is highly regarded in both industry and academia [56], is employed here for numerical simulations. In the process of solving partial differential equations using the finite volume method, we divide the computational domain into a finite number of control volumes to more accurately capture and analyze the complex behavior of fluids. The pimpleFoam solver is specifically designed for addressing unsteady Navier-Stokes equations. It integrates the Semi-Implicit Method for Pressure-Linked Equations (SIMPLE) with the Pressure-Implicit with Splitting of Operators (PISO) algorithms [57, 58]. This integration enables the effective resolution of complex, time-dependent flow scenarios, allowing for larger time steps while maintaining both stability and computational efficiency.

B. Circular cylinder environment

The configuration used for simulating flow around a circular cylinder closely follows the classical benchmark established by [59]. As illustrated in figure 1, the cylinder is placed within a rectangular computational domain with dimensions of $22D$ along the x -axis and $4.1D$ along the y -axis. The origin of the Cartesian coordinate system is positioned at the center of the cylinder. The cylinder is slightly offset in the y -direction to induce vortex shedding, facilitating the analysis of oscillatory flow phenomena. The boundaries of the computational domain are divided into an inlet Γ_{in} , an outlet Γ_{out} , no-slip walls Γ_{w} , and two separate jets on the cylinder Γ_i ($i = 1, 2$), as shown in figure 1(a). At the inlet Γ_{in} , the inflow velocity along x -axis is prescribed by a parabolic velocity profile in the form,

$$U_{\text{inlet}}(y) = U_m \frac{(H - 2y)(H + 2y)}{H^2}, \quad (2)$$

and that along y -axis is prescribed as,

$$V_{\text{inlet}}(y) = 0. \quad (3)$$

U_m is the maximum velocity magnitude of the parabolic profile, and $H = 4.1D$ represents the total height of the rectangular domain. The average inlet velocity \bar{U} , is related to the parabolic velocity profile $U_{\text{inlet}}(y)$ through the expression:

$$\bar{U} = \frac{1}{H} \int_{-H/2}^{H/2} U_{\text{inlet}}(y) dy = \frac{2}{3} U_m. \quad (4)$$

Flow control on the cylinder surface is achieved by introducing synthetic jets at the top and bottom points, as shown in figure 1(b). These jets, denoted as Γ_i ($i = 1, 2$), can inject or suction fluid to control the flow around the cylinder. Each jet spans an angular

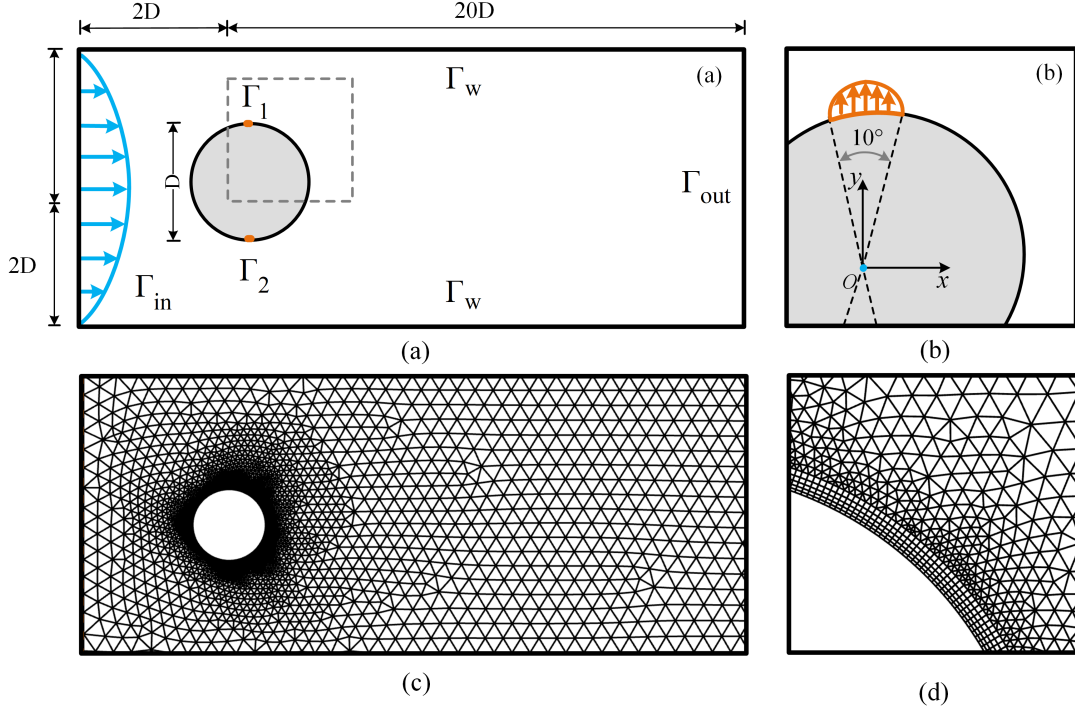


FIG. 1: Numerical simulation model of flow around a cylinder. (a) Domain configuration and boundary conditions. (b) Details of the jets conditions on the cylinder. Jets are located at $\Omega = 90^\circ$ and $\Omega = 270^\circ$ on the cylinder, with a jet width of $\omega = 10^\circ$. Parabolic velocity distribution is used for each jet. (c) Mesh structure around the object, and (d) Zoomed-in view of the mesh near the cylinder boundary.

width of $\omega = 10^\circ$ and is oriented perpendicularly to the outer surface of the cylinder. The velocity profile within each jet follows a parabolic distribution, allowing for both positive (blowing) and negative (suction) velocities. A key aspect of the AFC implementation is ensuring mass conservation within the system. This is achieved by balancing the net mass flow rates of the jets, i.e., $V_{\Gamma_1} = -V_{\Gamma_2}$, which ensures that the net flow into or out of the system remains zero.

Additionally, a no-slip boundary condition is enforced on the areas of the cylinder surface where the jets are not located, preventing any relative motion between the fluid and the cylinder in those regions. At the outlet boundary Γ_{out} , an outflow condition is applied, where the velocity is extrapolated based on the internal flow field. No-slip boundary conditions are also applied at the upper and lower walls Γ_w , ensuring that the velocity at these walls is zero relative to the boundary surface. This specification of boundary conditions ensures accurate flow simulation and effective control through synthetic jets. Mathematically, the boundary conditions are written as:

$$\begin{aligned}
 -\rho \mathbf{n} \cdot \mathbf{p} + Re^{-1} (\mathbf{n} \cdot \nabla \mathbf{u}) &= 0 & \text{on } \Gamma_{out}, \\
 \mathbf{u} &= 0 & \text{on } \Gamma_w, \\
 \mathbf{u} &= U & \text{on } \Gamma_{in}, \\
 \mathbf{u} &= f_{Q_i} & \text{on } \Gamma_i, \quad i = 1, 2.
 \end{aligned} \tag{5}$$

where, \mathbf{n} denotes the normal vector and f_{Q_i} represents the radial velocity profiles simulating the suction or injection of fluid by the jets.

To thoroughly investigate the impact of synthetic jets positioning on flow control performance around a circular cylinder, a series of experiments is conducted, employing various jet configurations: one pair, two pairs, and three pairs of jets. In the single-pair configuration, five different jet placement schemes are examined to evaluate their effectiveness in controlling the flow. Each scheme is designated according to the position of the jets. For example, J_1^1 and J_1^2 refer to a pair of synthetic jets symmetrically positioned about the x -axis, with a net mass flow rate of zero across the pair. In the notation J_1^1 , the subscript 1 indicates the first pair of synthetic jets, while the superscript 1 designates the first jet within that pair. For each jet placement scheme, the azimuthal angles of the first jet in each pair are indicated in the figures. The configurations analyzed include jets positioned at angles of 60° , 75° , 90° , 105° , and 120° . For the two-pair configuration, we explore two different placement schemes to evaluate the interaction effects between multiple pairs of jets. The three-pair configuration involves a specific arrangement designed to provide deeper insights into the cumulative effects of additional jet pairs on flow control. In this configuration, flow

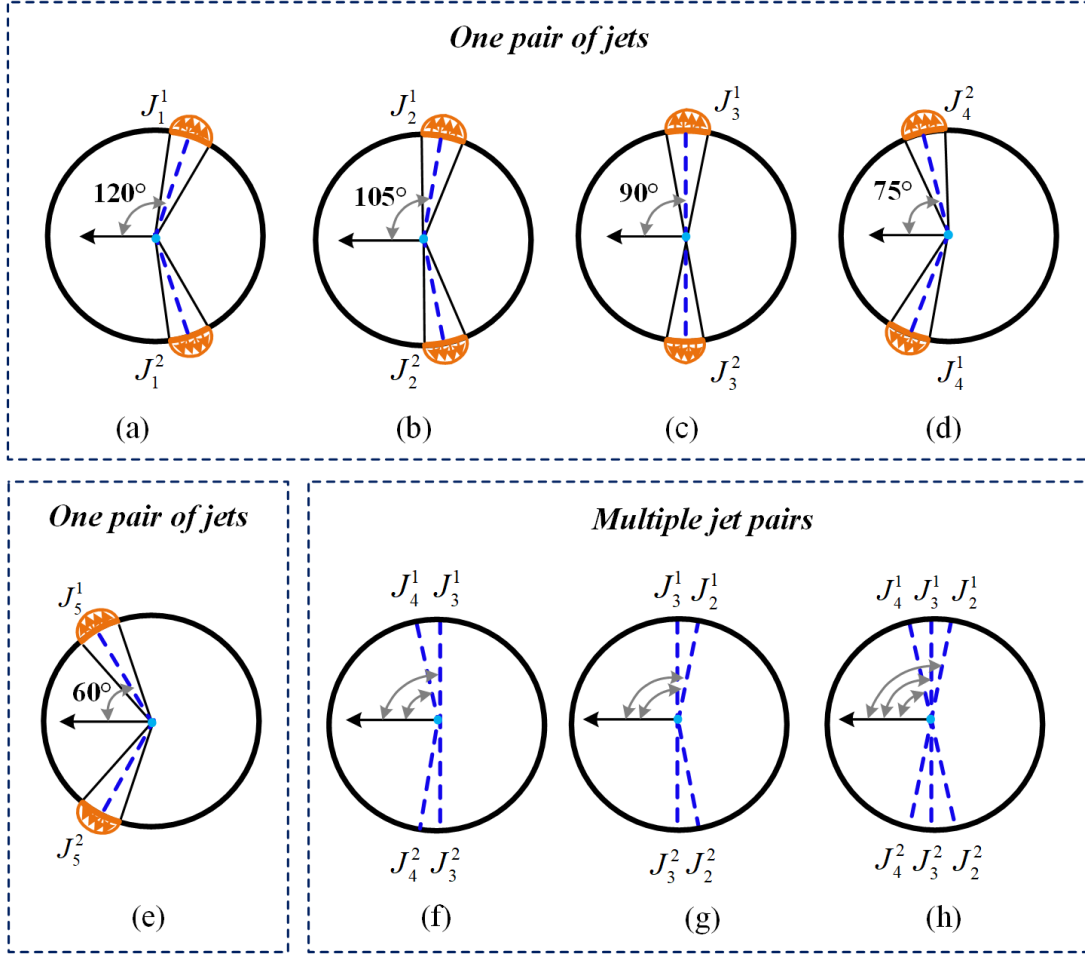


FIG. 2: For a single pair of jets, five different arrangements are considered: (a) J_1^1 and J_1^2 , (b) J_2^1 and J_2^2 , (c) J_3^1 and J_3^2 , (d) J_4^1 and J_4^2 , (e) J_5^1 and J_5^2 . For two pairs of jets, two arrangements are examined: (f) J_1^1, J_3^1, J_4^1 , and J_2^2 ; (g) J_1^1, J_3^1, J_2^1 , and J_2^2 . For three pairs of jets, one arrangement is studied: (h) $J_2^1, J_2^2, J_3^1, J_3^2, J_4^1$, and J_4^2 .

control is achieved by simultaneously activating $J_2^1, J_2^2, J_3^1, J_3^2, J_4^1$, and J_4^2 . The precise locations and nomenclature of these jets are detailed in figure 2.

In scenarios involving multiple jet pairs, it is important to emphasize that the control strategy derived from DRL assigns distinct actions to each individual pair of jets. This approach allows the agent to assign distinct action values to jets positioned at various locations, facilitating tailored control that considers the unique dynamics associated with each jet placement. By assigning unique actions to each jet pair, the DRL framework facilitates the evaluation of the relative effectiveness of flow control at different positions. This method enables the quantification of the contribution of each jet pair to the overall control strategy, providing a deeper understanding of the role each jet plays in modulating the flow dynamics. The objective of this study is to develop a DRL-based control strategy that enables simultaneous flow control at multiple positions on the cylinder. By assigning distinct actions to each individual jet pair, the agent can tailor the control to the specific dynamics associated with the placement of each jet. This approach allows for a systematic comparison of jet performance at various locations, facilitating the evaluation of the relative effectiveness of flow control across different positions. Furthermore, this comparison is complemented by an analysis of the underlying causes of observed performance differences, informed by principles of fluid mechanics. Such a comprehensive analysis enhances our understanding of how the contribution of each jet is influenced by its position and the physical mechanisms governing the flow dynamics.

C. Square cylinder environment

The computational domain for simulating the flow around a square cylinder is precisely defined with dimensions of $40D \times 20D$, where D represents the characteristic side length of the cylinder. The origin is located at the center of the cylinder, with $10D$

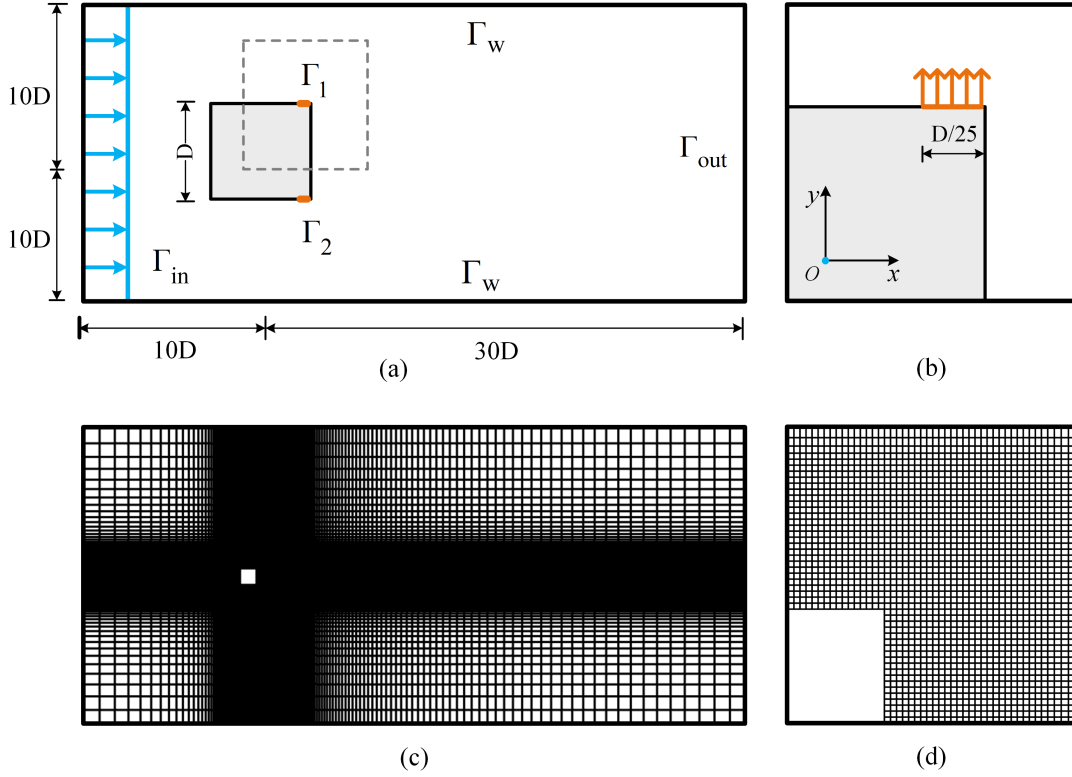


FIG. 3: Schematic of the computational domain and boundary conditions. (a) Establishment of the coordinate system and detailed dimensions of the computational domain. (b) Placement of the synthetic jets near the trailing corner point. (c) The mesh generation scheme around the square object, illustrating the distribution of high-density mesh in regions prone to flow separation, and (d) A close-up view of the mesh structure, highlighting the refinement near the boundary layer.

extending both above and below this point to define the vertical boundaries. The domain extends $10D$ upstream from the cylinder to the inlet boundary Γ_{in} , providing sufficient distance for the flow to fully develop into a uniform profile before interacting with the cylinder. Downstream, the domain stretches $30D$ from the cylinder to the outlet boundary Γ_{out} , ensuring ample space for capturing the wake formation and vortex shedding phenomena. As illustrated in figure 3(a), this spatial configuration is carefully optimized to minimize the influence of boundary effects on the flow around the cylinder while ensuring that the downstream region is sufficiently extended to capture the wake dynamics with high accuracy. This design is critical for maintaining the fidelity of the numerical simulations and ensuring the robustness and reliability of the results.

In the simulation setup, the inlet of the computational domain is prescribed with a uniform velocity profile, where the velocity magnitude is set to 2 and aligned along the x -axis. The synthetic jets are configured with velocities perpendicular to the walls of the square cylinder, directed along the outward normal to these walls, as illustrated in figure 3(b). Except at the locations of the synthetic jets, the remaining sections of the square cylinder walls are subjected to no-slip solid wall boundary conditions, ensuring that the fluid adheres to the surfaces and accurately reflecting the physical constraints imposed by solid boundaries on the fluid flow. At the outlet boundary, Neumann-type conditions are applied to maintain a zero stress vector, effectively simulating the natural flow behavior at an infinite distance. The upper and lower boundaries of the domain are defined with far-field boundary conditions, designed to minimize their impact on the flow around the square cylinder and closely approximate an unbounded fluid domain. This careful configuration ensures the accuracy and reliability of the simulation, allowing for a precise investigation of the flow dynamics.

To ensure numerical stability, the time step size is carefully selected as $\Delta t = 0.0005$ following extensive validation and iterative testing. This choice balances temporal accuracy with adherence to the CFL condition, particularly in regions of high flow velocity and steep gradients. The rigorous selection of this parameter minimizes numerical errors, thereby enhancing the fidelity of the simulation and ensuring a reliable analysis of the fluid dynamics. The mesh topology surrounding the square cylinder is illustrated in figure 3(c). The global mesh is designed to systematically coarsen with increasing radial distance from the cylinder, optimizing computational efficiency while maintaining accuracy. In contrast, figure 3(d) highlights the local mesh refinement near the cylinder, where the grid undergoes significant densification to form high-resolution elements. This local refinement is essential for accurately capturing the intricate flow dynamics within the boundary layer, particularly in areas with elevated shear and steep velocity gradients. Such precision in mesh design is crucial for resolving critical flow phenomena and ensuring the

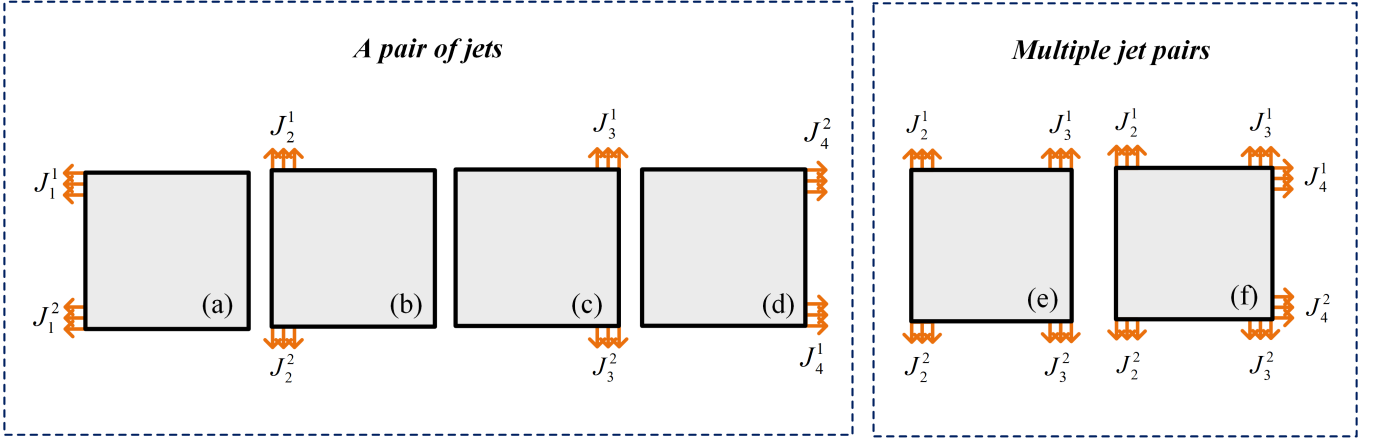


FIG. 4: Jets arrangement schemes for the flow around a square cylinder. For a single pair of jets, five different arrangements are considered: (a) J_1^1 and J_1^2 ; (b) J_2^1 and J_2^2 ; (c) J_3^1 and J_3^2 ; (d) J_4^1 and J_4^2 . For two pairs of jets, two arrangements are examined: (e) J_2^1, J_2^2, J_3^1 and J_3^2 ; For three pairs of jets, one arrangement is studied: (f) $J_2^1, J_2^2, J_3^1, J_3^2, J_4^1$ and J_4^2 .

overall reliability of the simulation results.

To investigate the impact of synthetic jets positioning on the flow control performance around a square cylinder, we design a series of experiments with different jet configurations: one pair of jets, two pairs of jets, and three pairs of jets. In the one-pair jet configuration, we explore four different jet placement schemes. Each scheme involves a distinct spatial arrangement to assess the optimal positioning for effective flow control. The four different jet placement schemes are named according to the location of the synthetic jets. For instance, J_1^1 and J_1^2 represent a pair of jets located near the front corners of the square cylinder, where the subscript 1 indicates the first pair of synthetic jets, which has a net mass flow rate of zero. The superscript 1 or 2 is used to distinguish between the two different jets within the pair. For the two-pair jet configuration, we investigate a single jet placement scheme aimed at analyzing how two strategically positioned pairs of jets influence the flow dynamics. Similarly, for the three-pair jet configuration, we examine a specific jet placement scheme to understand the effects of three pairs of jets on flow control performance. The precise positions and designations of the jets for each configuration are detailed in figure 4. Notably, in scenarios involving multiple pairs of jets, the control strategy derived from DRL provides distinct control actions for each individual pair of jets. This approach allows for a nuanced assessment of how different configurations and placements of synthetic jets influence the overall control effectiveness in modifying the flow around the square cylinder.

D. Deep Reinforcement Learning

Deep learning is a critical branch of machine learning, with its core centered on utilizing the multi-layered structure of artificial neural networks to process and analyze data. This multi-layered structure, also known as deep neural network, consists of an input layer, multiple hidden layers, and an output layer [60]. The input layer receives raw data, such as image pixels or text word vectors, and introduces these features into the network. The hidden layers, positioned between the input and output layers, are composed of interconnected neurons and are responsible for the layer-by-layer processing and transmission of information. The output layer generates the final prediction results or classification labels, with its structure and the number of neurons tailored to the specific task [61]. Through this layered processing and non-linear transformations, DNN can automatically extract complex features from raw data and capture intricate patterns, enabling deep learning to exhibit exceptional performance in tasks such as image recognition, natural language processing, and speech recognition.

Reinforcement Learning is a sophisticated machine learning paradigm that emphasizes empowering an agent to autonomously learn optimal actions within a dynamic environment through a process of trial and error [11]. The objective of the agent is to maximize cumulative rewards over time by continuously interacting with the environment, receiving feedback in the form of rewards or penalties, and incrementally refining the strategy to make increasingly effective decisions [62]. Through this iterative process, the agent adapts to the complexities of the environment and discovers the most advantageous actions to achieve long-term goals, ultimately enhancing its ability to make informed and efficient decisions across a wide range of scenarios.

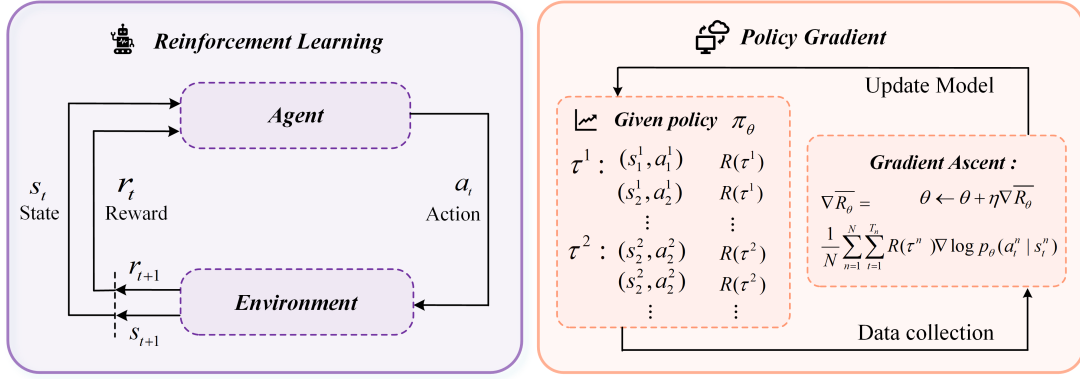


FIG. 5: Basic structures of (a) Reinforcement Learning and (b) Policy gradient.

1. Foundation

The agent is the entity that executes actions, learning and optimizing its strategy through repeated interactions with the environment, as depicted in figure 5(a), which illustrates the basic structure of agent-environment interaction. The environment serves as the external system within which the agent operates, providing feedback in the form of rewards based on the actions taken by the agent ($a \in \mathbb{A}$) [10]. The state ($s \in \mathbb{S}$) represents a snapshot of the environment at a specific moment, typically perceived by the agent as information from the environment. The agent uses a policy ($\pi(a|s)$), which is a set of rules or a function that guides the selection of actions based on the current state. The policy can be either deterministic or stochastic. The state value function ($V(s)$) evaluates the desirability of a particular state, representing the expected cumulative reward that can be obtained starting from that state. Similarly, the action value function ($Q(s, a)$) assesses the desirability of taking a specific action in a given state, representing the expected cumulative reward that can be achieved by executing that action in the state [62].

2. Mathematical model

RL fundamentally relies on the concept of a finite markov decision process (MDP) to model the decision-making process [63, 64]. A finite MDP is characterized by the tuple (S, A, P, R, γ) , where S represents the finite state space, A denotes the finite action space, P is the state transition probability function, and R is the reward function. The discount factor γ quantifies the relative importance of future rewards compared to immediate rewards [63]. At each time step i , the agent observes the environment in state s_i , selects an action a_i , and transitions to the next state s_{i+1} with probability $p(s_{i+1}|s_i, a_i)$. The agent then receives a reward $R(s_i, a_i, s_{i+1})$ associated with this transition. The decision-making process is governed by a policy $\pi(a_i|s_i)$, which specifies the probability of choosing action a_i given the current state s_i [64].

3. Classification

RL can be broadly categorized into two main types: value-based methods and policy-based methods. Value-based methods involve learning a $V(s)$ or a $Q(s, a)$ that estimates the expected cumulative reward for a given state or state-action pair [15, 64]. The agent selects the optimal action by maximizing these value functions, with examples including Q-learning and DQN [65]. Policy-based methods, on the other hand, directly learn a policy function ($\pi(a|s)$), which represents the probability distribution of selecting actions given a particular state [15, 66]. The agent optimizes the policy function to maximize cumulative rewards, making this approach effective in handling continuous action spaces and stochastic policies. Common policy-based algorithms include policy gradient methods [67], trust region policy optimization (TRPO) [68], and PPO [12]. The basic training structure of policy-based algorithms is illustrated in figure 5(b).

DNNs are a class of machine learning models composed of multiple layers of interconnected neurons, capable of automatically learning and extracting features from data [60]. They excel in handling complex, high-dimensional datasets, making them essential for tasks such as image recognition, natural language processing, and reinforcement learning. In the framework of DRL, where DL plays a central role, the combined operation of DL and RL is depicted in figure 6. By using DNNs, deep learning can automatically extract key features from complex and high-dimensional data, significantly enhancing the ability of reinforcement learning to deal with complex environments. The functional representation ability of deep learning is extremely powerful, especially in policy representation and value function approximation, where it plays a crucial role. These capabilities enable

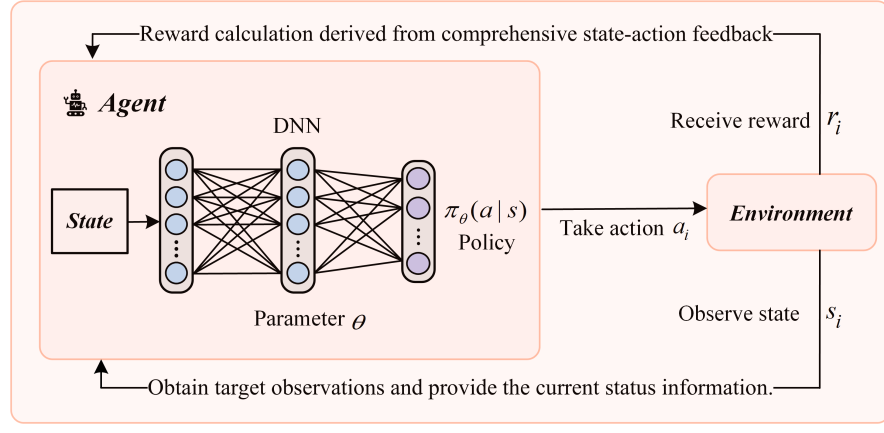


FIG. 6: Basic structures of deep reinforcement learning.

DRL to achieve more accurate and efficient decision-making in high-dimensional, continuous action spaces, greatly improving its application effect and breadth in complex decision-making environments [8].

In reinforcement learning, the $V(s)$ and the $Q(s, a)$ are used to evaluate the goodness of a state or a state-action pair, typically represented in terms of cumulative rewards. The $V(s)$ represents the expected cumulative reward that can be obtained starting from state s and following a policy π [69]. It is defined as:

$$V(s) = \mathbb{E}_\pi \left[\sum_{t=0}^{\infty} \gamma^t r_t \mid s_0 = s \right], \quad (6)$$

where \mathbb{E}_π denotes the expectation under the policy π . γ is the discount factor, $0 \leq \gamma \leq 1$, which discounts future rewards. r_t is the immediate reward received at time step t . $s_0 = s$ indicates that the initial state is s .

The action value function $Q(s, a)$ represents the expected cumulative reward that can be obtained by taking action a in state s and subsequently following the policy π . It is defined as:

$$Q(s, a) = \mathbb{E}_\pi \left[\sum_{t=0}^{\infty} \gamma^t r_t \mid s_0 = s, a_0 = a \right], \quad (7)$$

where \mathbb{E}_π similarly denotes the expectation under the policy π . γ is the discount factor. r_t is the immediate reward received at time step t . $s_0 = s$ indicates that the initial state is s , and $a_0 = a$ indicates that the initial action is a . These two functions together describe the expected cumulative rewards associated with different states and state-action pairs, helping the agent optimize its policy to maximize long-term returns.

The advantage function $A(s, a)$ is typically computed based on the $V(s)$ and the $Q(s, a)$. The advantage function $A(s, a)$ evaluates the relative benefit of taking action a in a given state s compared to other possible actions [70]. The standard formula is:

$$A(s, a) = Q(s, a) - V(s), \quad (8)$$

where $Q(s, a)$ is the action value function, representing the expected cumulative reward for taking action a in state s . $V(s)$ is the state value function, representing the expected cumulative reward for being in state s without considering which action is taken.

PPO is a powerful policy optimization algorithm that maintains the stability of policy performance by limiting the amplitude of policy updates. It uses a proxy objective function to encourage policy updates so that the probability ratio of the current policy to the old policy remains within a certain range, thereby avoiding drastic fluctuations in policy performance. Also, PPO uses the advantage function to evaluate the advantage of state-action pairs, and optimizes the proxy objective function through stochastic gradient descent, ultimately finding the optimal policy that can obtain the highest expected cumulative reward [12].

$$L^{\text{CLIP}}(\theta) = \hat{\mathbb{E}}_t \left[\min \left(\frac{\pi_\theta(a_t|s_t)}{\pi_{\theta_{\text{old}}}(a_t|s_t)} \hat{A}_t, \text{clip} \left(\frac{\pi_\theta(a_t|s_t)}{\pi_{\theta_{\text{old}}}(a_t|s_t)}, 1 - \epsilon, 1 + \epsilon \right) \hat{A}_t \right) \right], \quad (9)$$

where $L^{\text{CLIP}}(\theta)$ is used to optimize the performance of the current policy, where $\hat{\mathbb{E}}_t$ denotes the empirical expectation at time step t . The ratio of the probability of choosing action a_t under the current policy $\pi_\theta(a_t|s_t)$ to the probability under the old

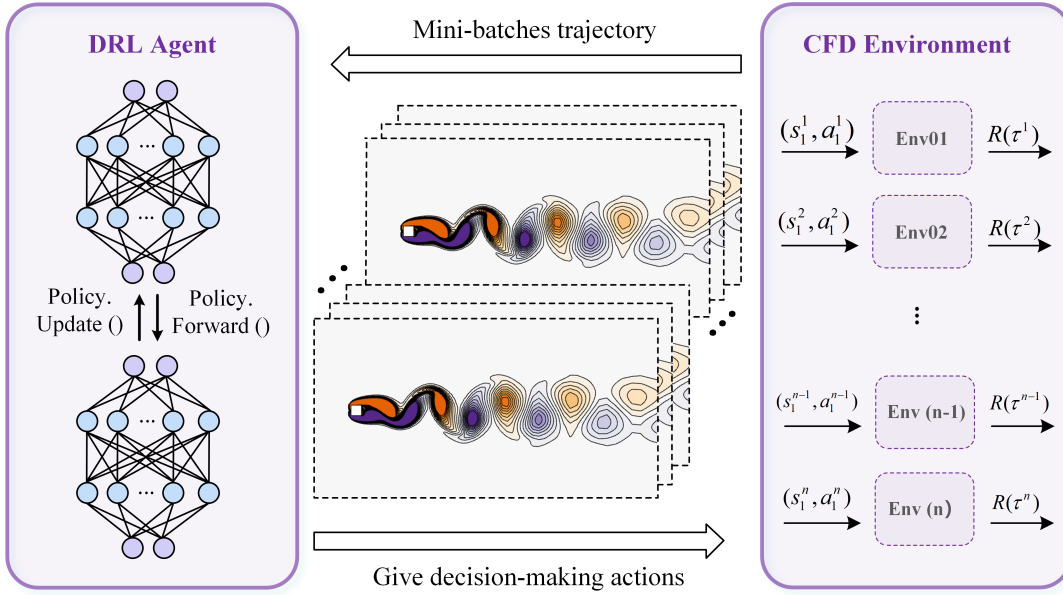


FIG. 7: Schematic of the interaction between the deep reinforcement learning agent and the computational fluid dynamics environment for active flow control. The DRL agent receives state information s_t^i from the CFD environment at each timestep t , selects an action a_t^i to adjust the synthetic jets, and then the environment returns a new state s_{t+1}^i and a reward $R(\tau^i)$, where τ^i represents the trajectory of states and actions. The agent updates its policy π_θ to maximize the expected cumulative reward $\mathbb{E}[R(\tau^i)]$, optimizing flow control through iterative learning across multiple parallel environments.

policy $\pi_{\theta_{\text{old}}}(a_t | s_t)$ is represented as $\frac{\pi_\theta(a_t | s_t)}{\pi_{\theta_{\text{old}}}(a_t | s_t)}$, which measures the extent of policy change. The advantage function estimate \hat{A}_t evaluates the relative value of taking action a_t in state s_t . To maintain stability in policy updates, a clipping mechanism is introduced: $\text{clip}\left(\frac{\pi_\theta(a_t | s_t)}{\pi_{\theta_{\text{old}}}(a_t | s_t)}, 1 - \epsilon, 1 + \epsilon\right)$, which restricts the policy ratio within the range $[1 - \epsilon, 1 + \epsilon]$, where ϵ is a small hyperparameter controlling the range of the update. The objective function enables the PPO algorithm to achieve stable policy updates while enhancing policy performance. The key components and parameter configurations of the PPO algorithm are elaborated in Appendix.

E. DRL-Enhanced Active Flow Control

A computational fluid dynamics environment is coupled with a DRL framework to address AFC. The two core components of DRL, the agent and the environment, are integral to this approach. In our study, we utilize a PPO agent to train the control policy, while the CFD environment simulates flow around either a circular or square cylinder. The primary task of the PPO agent is to determine an optimal real-time control strategy for two jet actuators positioned on the cylinder's surface, with the goal of minimizing the fluid forces acting on the structure. The agent obtains state information by observing the CFD environment, with flow probes measuring quantities such as velocity and pressure within the flow field. The agent's actions involve adjusting the mass flow rate of the synthetic jets, enabling precise control over the flow dynamics. To present a clear understanding of the DRL-based AFC framework, we provide a detailed explanation of each key component: the agent, the environment, state observations, action selection, and the reward mechanism. By elaborating on these elements, we aim to clarify their roles within the system and illustrate how they interact. This detailed breakdown enhances our ability to analyze and understand the application of DRL in optimizing AFC performance.

- **Agent** : The neural network of the agent is parameterized by θ (including weights and biases), and through training, this network learns the optimal policy $\pi_\theta(a_t | s_t)$, which represents the probability distribution of actions a_t given a state s_t . The objective is to maximize the expected cumulative reward $R_t = \sum_{k>t} \gamma^{(k-t)} r_k$, where $\gamma \in (0, 1]$ is the discount factor. PPO is an episode-based actor-critic algorithm that includes both an actor network π_θ and a critic network $V(s_t)$. In the PPO algorithm, the actor network is responsible for learning and outputting the policy $\pi_\theta(a_t | s_t)$ for selecting actions in different states to maximize the cumulative reward R_t . The critic network $V(s_t)$ evaluates the expected cumulative reward for each state s_t and provides feedback and guidance for updating the policy π_θ of the actor network. Both the actor and critic networks are comprised of two fully connected layers, each with 512 units. The Adam optimizer is used for updating

the networks, with a fixed learning rate of 0.001. In reinforcement learning, agent selection depends on the state space, action space, exploration-exploitation trade-off, computational resources, and objectives. For high-dimensional continuous spaces like fluid mechanics, PPO [17, 23, 24], SAC [25, 32, 37], TD3 [71] and TQC [32] are ideal, with PPO excelling in real-time flow control due to its exploration balance and efficiency.

- **Environment** : the environment interacting with the agent is instantiated using CFD. The gym library interface is utilized to integrate OpenFOAM into the DRL framework. The CFD simulations are performed using the open-source software platform OpenFOAM® version 8. Figure 7 illustrates the integration of CFD computations as a DRL training environment and demonstrates the benefits of accelerating the training process by using multiple parallel CFD environments. This parallelization strategy is inspired by the work of [35], and also incorporates insights from [36]. Research by [35] indicates that acceleration can be achieved by parallelizing both the numerical simulations and the DRL algorithm. In their study, CFD computations utilized the finite element method implemented within the FEniCS framework. [36] demonstrated that different CFD computation platforms can significantly affect parallel acceleration. They investigated various hybrid parallelization configurations based on the OpenFOAM environment and proposed effective parallelization strategies. This study involves two flow scenarios: flow around a square cylinder and flow around a circular cylinder, which were described in detail in the previous sections. The environment depends on the type of CFD solver, and there are various codes available for coupling numerical simulation environments with RL frameworks. For example, RL has been integrated with the FEniCS environment [23], the OpenFOAM environment [37], and the Nek5000 environment [31].
- **Action a_t** : In the interaction between the agent and the environment, the actions are defined as the dimensionless mass flow rates of the synthetic jets Q_i ($i = 1, 2$). To maintain a zero net mass flow rate in the system, a mass balance constraint $Q_1 + Q_2 = 0$ is imposed. This constraint not only ensures the physical conservation of mass but also significantly enhances the stability of the numerical simulations by mitigating errors associated with imbalanced flows. Furthermore, to prevent non-physical large actuation that could destabilize the system, a limit is imposed on the normalized mass flow rate, such that $|Q_i^*| < 0.06$. Q_i^* denotes the normalized mass flow rate, defined as Q_i/Q_{ref} , where $Q_{\text{ref}} = \int_{-D/2}^{D/2} \rho U(y) dy$ serves as the reference mass flow rate, based on the fluid density and velocity distribution. This constraint effectively regulates the jet intensity, thereby ensuring both stability and accuracy in the flow control process, leading to more precise and reliable numerical results. To further ensure stability and mitigate non-physical instabilities in the flow, a smoothing function is applied, where V_{Γ_1, T_i} represents the jet velocity at the end of the i th actuation control period T_i , and β is a numerical smoothing parameter:

$$V_{\Gamma_1, T_i} = V_{\Gamma_1, T_i} + \beta (a - V_{\Gamma_1, T_{i-1}}). \quad (10)$$

- **State s_t** : The agent observes the state of the CFD environment by collecting physical field data from specific locations within the computational domain. Building on previous studies, such as those by [27], who utilize velocity probes, and [23], who employ pressure probes to capture instantaneous pressure at key points, we draw inspiration from [31] to strategically place observation probes at locations within the flow field where fluctuations are most pronounced. These probes are situated in regions of the wake characterized by the weakest stability and highest sensitivity, allowing for more effective flow control through the monitoring of time-averaged fluctuating pressure. This targeted placement optimizes the control strategy by focusing on the most critical areas of the flow, thereby enhancing both the efficiency and effectiveness of the flow control efforts. In addition to positioning probes within the wake region, we also place probes around the circumference of the cylinder to extract physical information from its surface, which is closely related to the lift and drag on the cylinder. For more details on the number and distribution of these probes, readers can refer to the studies by [27, 31, 34], who have conducted in-depth discussions on this topic.
- **Reward r_t** : The design of the reward function is based on the overall objective of flow control, making the selection of appropriate performance metrics crucial for the convergence and stability of reinforcement learning. This work aims to achieve flow control for reducing both drag and lift around the cylinder. Therefore, we construct the reward function based on the drag coefficient (C_D) and the lift coefficient (C_L). The specific reward function is defined as follows:

$$r_{T_i} = C_{D,0} - (C_D)_{T_i} - \omega |(C_L)_{T_i}|, \quad (11)$$

where, $C_{D,0}$ represents the baseline drag coefficient, serving as a reference to encourage positive rewards and facilitate convergence during training. The term $(C_D)_{T_i}$ denotes the drag coefficient at time step T_i , with the objective of minimizing it relative to the baseline. The lift coefficient $(C_L)_{T_i}$ is also included, with its absolute value penalized to mitigate instabilities caused by lift around the bluff body. The parameter ω is a weighting factor used to balance the trade-off between reducing drag and controlling lift. Given the directional nature of the flow under consideration, ω is typically set between 0.1, 0.2 and 1, reflecting the relative importance of minimizing drag over controlling lift fluctuations. In previous work, the lift coefficient penalty factor is often set to 0.1 [36], 0.2 [23, 24], or 1 [26]. A penalty factor of 0.2 is used, consistent with [23].

- **Interaction:** In DRL, the interaction between the agent and the environment forms the foundation of the learning process. At each time step t , the agent first gathers physical data regarding the current flow state s_t from the CFD environment. Based on this information, the agent selects an action a_t according to its control policy $\pi_\theta(a_t | s_t)$. This selected action a_t is then communicated to the CFD environment, which executes the action, transitions to the next state s_{t+1} , and provides an immediate reward r_t . The agent, in turn, receives both the reward r_t and the updated physical state information s_{t+1} , using this feedback to refine its control policy π_θ in order to maximize cumulative future rewards $\sum_t \gamma^t r_t$, where γ is the discount factor. This iterative cycle continues until the task is accomplished or a predefined termination condition is met. Through successive interactions, the agent incrementally optimizes its control policy π_θ via trial and error, ultimately mastering the dynamic adjustment of jet velocity V_J in real-time to achieve optimal flow control performance. The total number of DRL training episodes is set to 3,000, with each episode consisting of 100 training timesteps. Each timestep corresponds to a non-dimensional time of 0.025, resulting in a maximum duration per episode of $T_{\max} = 2.5$. This duration spans approximately 8 to 10 vortex shedding cycles, during which 100 control actions are executed. Training the DRL agent over multiple vortex shedding cycles ensures that the agent fully captures the complex flow dynamics, stabilizes the learning process, and develops a robust and generalizable control strategy for effective flow management.

III. RESULTS: FLOW CONTROL PERFORMANCE OF A CIRCULAR CYLINDER

This section investigates how the positioning of synthetic jets influences flow control performance and associated costs, aiming to derive quantitative insights through rigorous physical analysis. The cost of implementing flow control is evaluated using the dimensionless mass flow rates of the synthetic jets. To systematically explore the effects of jet positioning, five configurations are designed with a single pair of synthetic jets, followed by two configurations involving two pairs of synthetic jets, and an additional configuration with a single pair of synthetic jets. During each training session, only the positions and numbers of the synthetic jets are varied, ensuring that any observed differences in convergence behavior are solely attributable to changes in actuator placement, with all other configuration parameters held constant.

A. A pair of synthetic jets controllers

1. Scenario A: Control Performance of Jet Pair

The performance and effectiveness of flow control strategies obtained through DRL training are compared for synthetic jets positioned at different locations on the cylinder surface. These five synthetic jets configurations are designed based on the angular positions on the cylinder, ranging from 60° to 120° . In these configurations, the J_1 setup includes two jets, J_1^1 and J_1^2 , with J_1^1 located at an angular position of 120° . The J_3 setup includes two jets, J_3^1 and J_3^2 , with J_3^1 located at 90° . The J_5 setup also includes two jets, J_5^1 and J_5^2 , with J_5^1 located at 60° .

The reward function curves reflect how the performance of the DRL agent evolves as training progresses, as shown in figure 8. In the early stages of training, the reward function curves often exhibit significant fluctuations, indicating the exploration and experimentation phase of the agent within the strategy space. As training continues, the agent gradually optimizes its strategy, leading to an upward trend in the reward function values, which suggests that the agent is effectively learning the flow control strategy. By comparing the learning curves for different jet positions, we observe that when the jets are positioned at J_1 , the reward function grows most slowly and reaches the lowest final value, indicating that the flow control strategy at this position is more challenging to converge. In contrast, when the jets are positioned at J_5 , the learning curve shows a slightly faster growth but still lags behind others, indicating a moderate difficulty in strategy convergence. Conversely, when the jets are positioned at J_2 , J_3 , and J_4 , the DRL agent achieves rapid convergence within 1,000 episodes, demonstrating that the flow control strategies at these positions are easier to learn and optimize. Between 1,000 and 3,000 episodes, the reward function curves plateau, indicating that the DRL agent has successfully mastered a stable and effective flow control strategy. At this stage, the reward values remain stable, further confirming the effectiveness and reliability of the learned strategy in reducing C_D and controlling C_L .

The baseline C_D represents the scenario without any active flow control and serves as a reference point. As shown in figure 8, all jet configurations achieve a reduction in C_D , with drag reduction of approximately 8% across the five jet positions. This indicates that the DRL-optimized jet actuation effectively reduces the drag experienced by the cylinder, with the curves stabilizing after the initial transient phase, suggesting that the control actions lead to a steady reduction in C_D . For the same jet configurations, the baseline C_L exhibits significant fluctuations, which are common in flows past bluff bodies such as cylinders. The DRL-controlled jets achieve a substantial reduction in these fluctuations, with the lift oscillations being nearly eliminated in all five jet positions, resulting in up to a 99% reduction in C_L oscillations. The dramatic reduction in lift fluctuations indicates that the jets not only reduce C_D but also stabilize the flow, preventing lift-induced instabilities that could otherwise affect the effectiveness of flow control. The stabilization of the C_D and C_L over time demonstrates that the learned strategies are both effective and stable. The

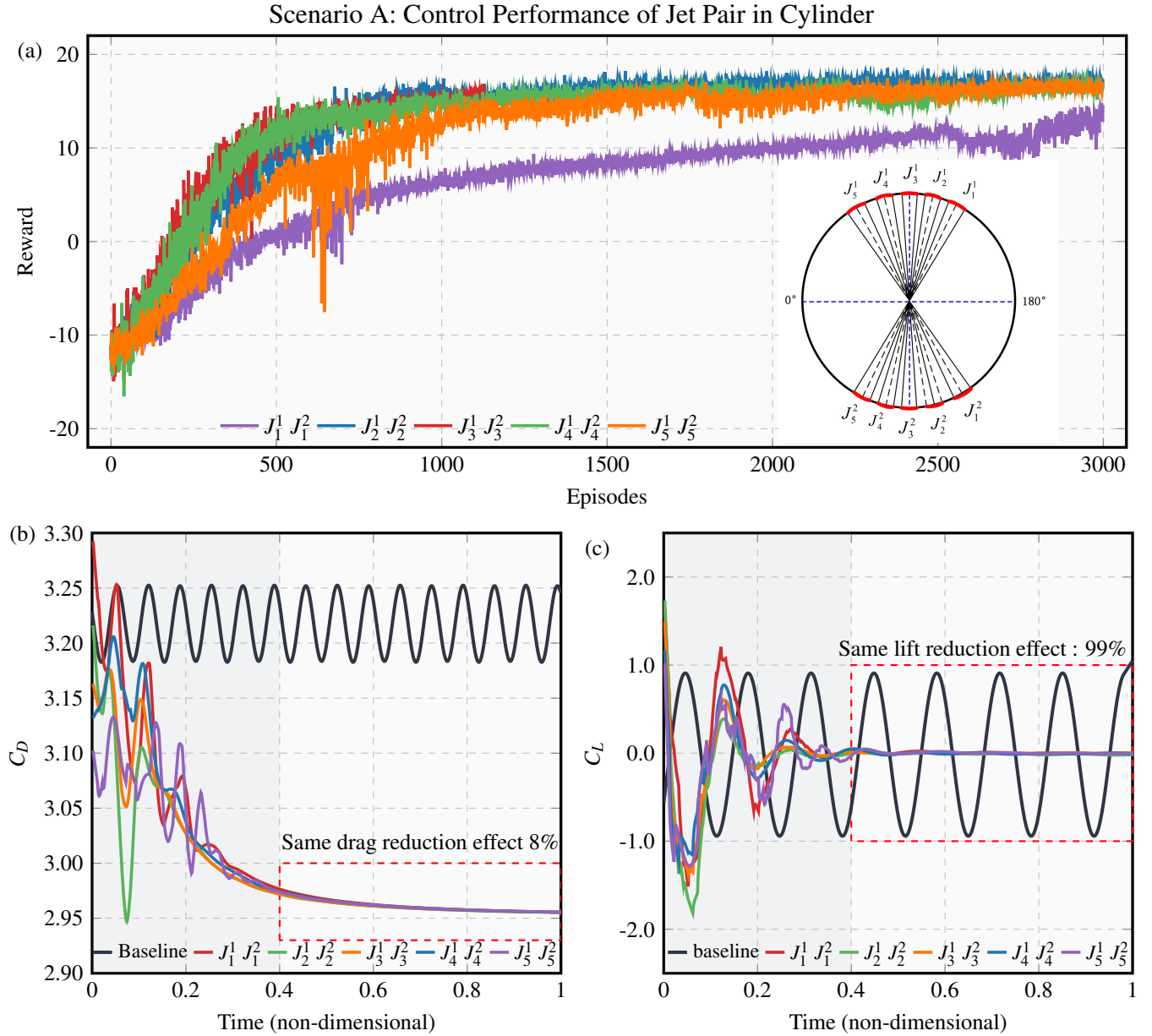


FIG. 8: Performance evaluation of different jets configurations for flow control around a cylinder. (a) Reward curves over training episodes for various jets positions. (b) C_D over non-dimensional time, comparing the baseline scenario with different jets configurations. (c) C_L over non-dimensional time, comparing the baseline scenario with different jets.

DRL training curves illustrate the learning process of the agent, resulting in an optimized control strategy that effectively reduces both C_D and C_L . The significant C_D reduction and near-complete suppression of lift fluctuations highlight the potential of DRL in achieving robust and efficient flow control in real-time applications.

The activation states of synthetic jets at various azimuthal angles, along with the corresponding controlled flow fields, are illustrated in figure 9. When the activation states of synthetic jets at different azimuthal angles are shown in the left column of figure 9, the pair of synthetic jets symmetric about the x-axis alternately engage in blowing or suction phases. With the jets positioned at J_1 at 120° , the velocity contours show the development of a large recirculation region on the cylinder's rear side, despite minor oscillations in the wake. When the jets are positioned at J_2 at 105° and J_3 at 90° , vortex shedding in the wake is fully suppressed, indicating that jets at these locations can effectively delay separation, reduce the separation zone, and even eliminate it, thereby reducing drag. For J_4 at 75° , the wake is largely stabilized, though weak oscillations persist downstream.

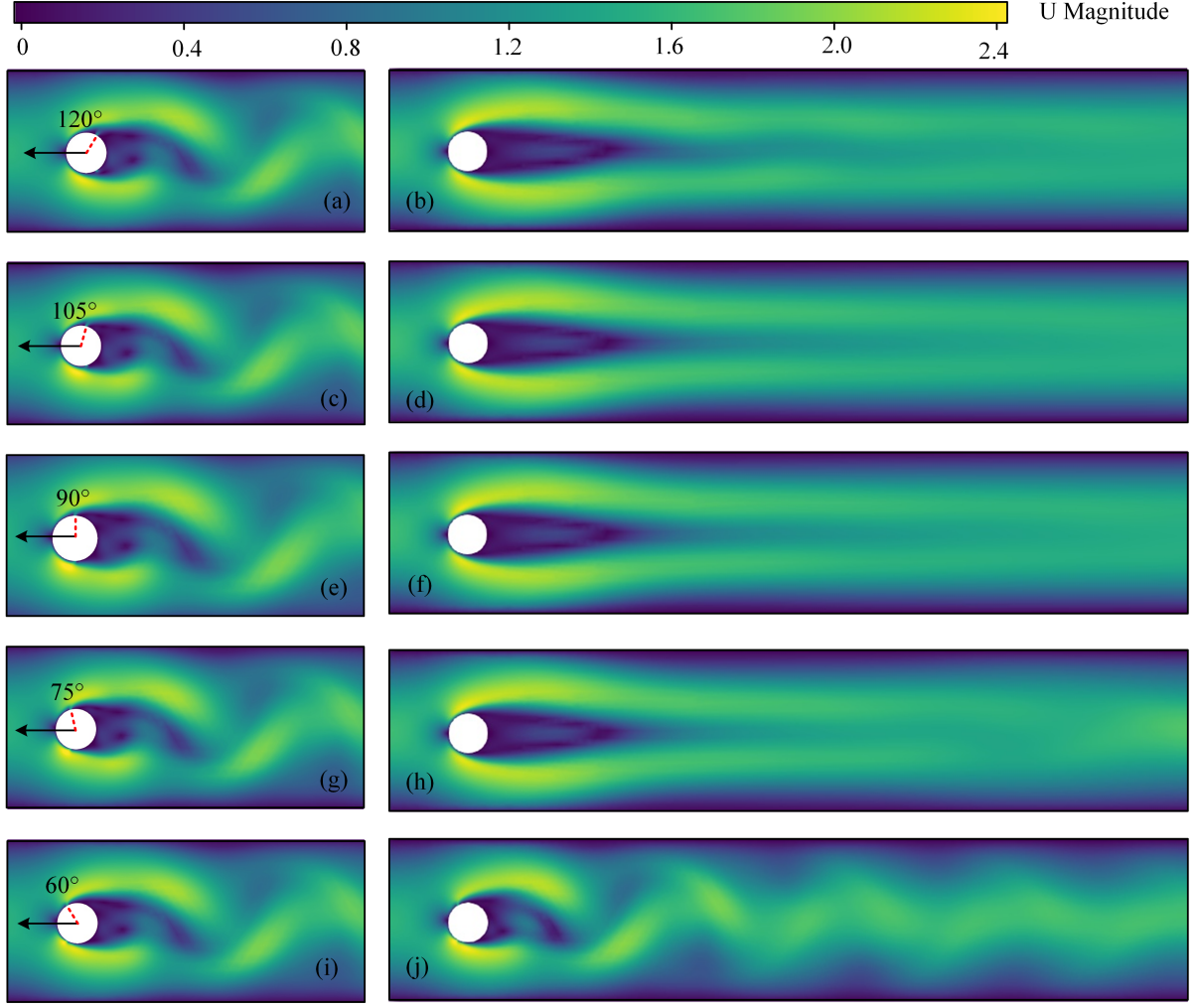


FIG. 9: Velocity contours of flow around a cylinder with synthetic jets at various angular positions. The left column shows the jet activation, and the right column shows the corresponding control results. (a) and (b) Jets at 120° , (c) and (d) at 105° , (e) and (f) at 90° , (g) and (h) at 75° , and (i) and (j) at 60° .

[72] used smoke flow visualization to show that a synthetic jet at an injection angle of $\gamma = 60^\circ$ caused local deformation of the streaklines on the upper surface of the cylinder, shifting the separation point downstream and the front stagnation point below the x-axis. When the jet is set at $\gamma = 60^\circ$, our reinforcement learning algorithm achieves similar control performance over the cylinder flow field as observed by [72], with periodic vortex shedding still evident in the controlled flow. The effectiveness of flow control varies significantly with jet positioning, with the least effective control observed at J_1 (120°) and J_5 (60°), where the jets can still delay separation.

2. Scenario A: Energy Consumption of Jet Pair

The analysis presented in figure 10 highlights the energy consumption and effectiveness of different jet configurations for flow control around the cylinder. The diagram depicts the angular positions of five pairs of injectors (J_1 to J_5) along the cylinder surface, with J_1 (60°) located closest to the upstream stagnation point (0°) and J_5 (120°) positioned further downstream. On the right side, the synthetic jet action values are displayed, representing the intensity of jet actuation. Control action values are plotted against dimensionless time for each configuration, providing deeper insights into the energy expenditure necessary to achieve the desired flow control. As depicted in figure 10, at the initial stage of flow control, the control effect curves of each jet configuration exhibit a peak, indicating the maximum energy required at the onset of jet actuation. Following this initial transient phase, the action values stabilize, suggesting that the control intensity and energy consumption become more stable and energy-efficient over time. Notably, the curves for J_5 and J_1 display the highest initial action values, indicating that these

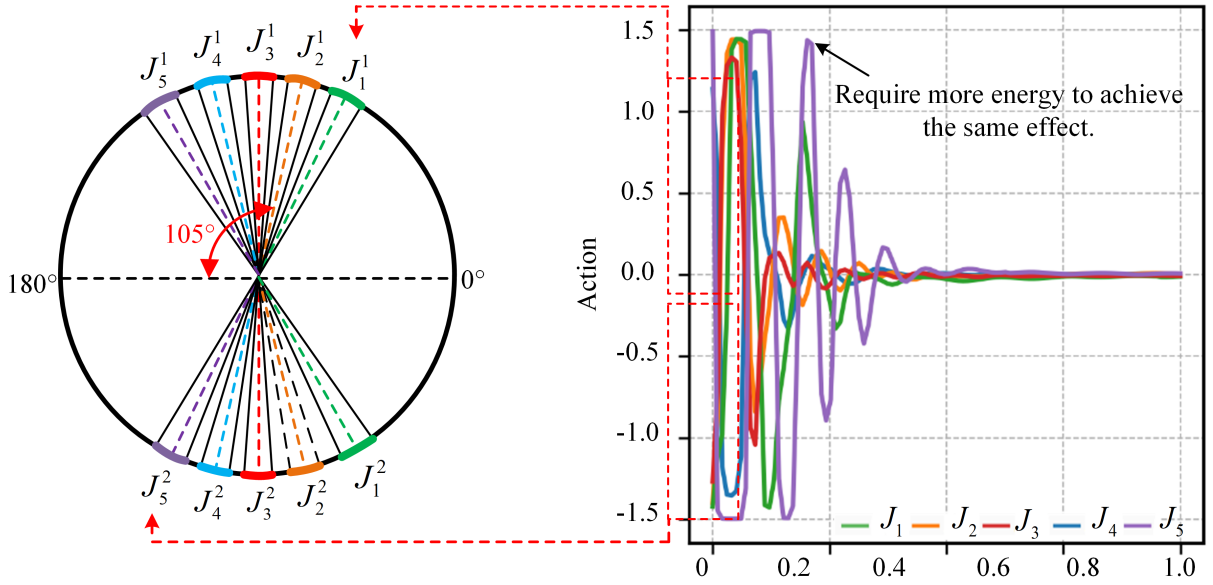


FIG. 10: Energy consumption analysis of jet pairs positioned at different angular locations around a cylinder. The left panel illustrates the angular placement of jet pairs J_1 through J_5 around the cylinder, while the right panel shows the corresponding action values over non-dimensional time for each jet configuration.

positions require more initial energy to initiate flow control compared to other configurations. In contrast, the action values for the synthetic jets positioned at J_2 , J_3 , and J_4 stabilize at a lower level than those of J_5 and J_1 , demonstrating that these configurations are more energy-efficient in maintaining flow control.

In the later stages of flow control, the synthetic jet at J_2 (105°) operates effectively with only 1% of the incoming flow rate, while those at J_1 (120°) and J_5 (60°) require over 3% to achieve comparable control performance. This disparity suggests that injectors positioned at 60° and 120° exhibit lower energy efficiency, necessitating a higher input to sustain the desired control effect. In contrast, injectors at 90° and 105° demonstrate superior efficiency, maintaining effective flow control with significantly lower energy consumption. Such findings highlight the importance of selecting optimal jet positions to minimize energy expenditure while achieving targeted flow control objectives. This insight highlights the critical importance of optimizing jet positioning to minimize energy consumption, a key consideration in designing efficient flow control systems that maximize aerodynamic performance while reducing power requirements around the cylinder.

B. Multiple pairs of synthetic jets controllers

1. Scenario B: Control Performance of Multiple Jets Control

Based on the results of flow control using a single pair of synthetic jets, it was observed that the configurations with jets positioned at 60° and 120° (J_5 and J_1) consumed the most energy. Consequently, when employing multiple pairs of synthetic jets for flow control, we excluded the jets positioned at 60° and 120°, focusing instead on combinations involving J_2 , J_3 , and J_4 . The configurations tested include two pairs of synthetic jets (J_2 and J_3 ; J_3 and J_4) and a configuration with three pairs (J_2 , J_3 , and J_4). To investigate the control performance and convergence speed of multiple synthetic jets combinations compared to single-pair synthetic jets, we analyze the control performance of single-pair synthetic jets (J_2 , J_3 , and J_4) as the control group. The performance of multiple jet configurations used for flow control around a cylinder, evaluated through deep Reinforcement Learning training, is comprehensively analyzed in figure 11(a). The reward curves reflect the effectiveness of the DRL agent in learning flow control strategies using different combinations of synthetic jets configurations. Across various configurations, the reward function exhibits a stepwise increase during the initial training phase. As training progresses, the reward values reach a plateau, indicating that the agent has successfully optimized its control strategy. However, different configurations display varying convergence speeds. It is observed that employing multiple pairs of synthetic jets for flow control does not accelerate the reinforcement learning training process. The reward function for single-pair synthetic jets converges more rapidly than that for multiple pairs, suggesting that single-pair jet configurations are more conducive to faster convergence and more effective for the agent to learn the control strategy.

The variation of the drag coefficient with non-dimensional time for different jet configurations is illustrated in figure 11(b).

Scenario B: Control Performance of Multiple Jets Control in Cylinder

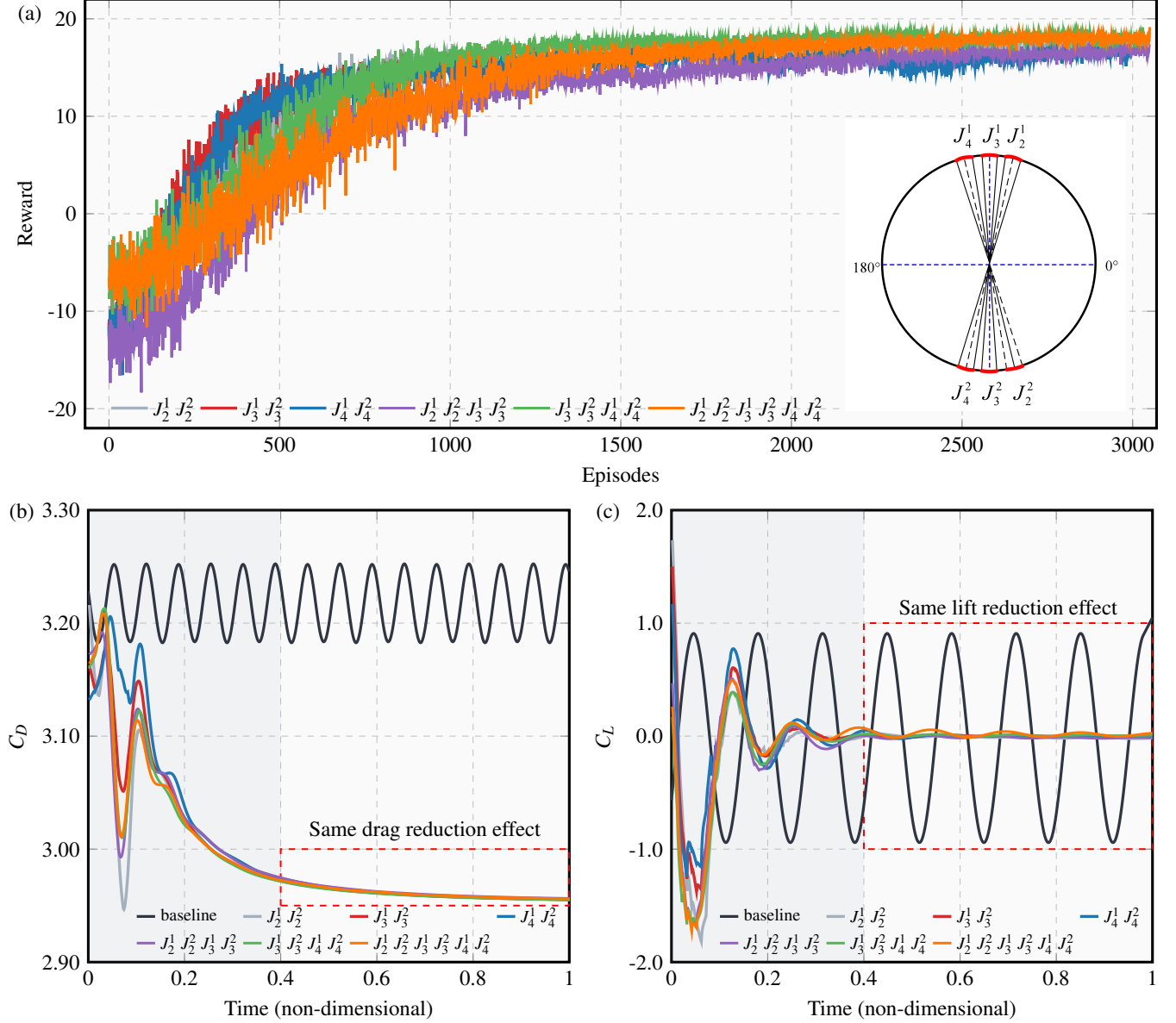


FIG. 11: Control performance evaluation of multiple jet configurations around a cylinder. (a) Reward curves over training episodes for various multi-jet configurations. (b) C_D over non-dimensional time. (c) C_L over non-dimensional time.

The curves indicate that all jet configurations achieve similar drag reduction, with the drag coefficient stabilizing after the initial transient phase. This stabilization suggests that the control strategies are effective in maintaining a consistent reduction in drag over time. The variation of the lift coefficient with non-dimensional time, demonstrating the effectiveness of the jet configurations in reducing lift fluctuations, is shown in figure 11(c). The results reveal a significant reduction in lift oscillations across all jet configurations, with the lift coefficient stabilizing near zero after the initial transient phase. Similar to the drag coefficient, the consistent performance across configurations reinforces the conclusion that these jet positions are effective and efficient for flow control. Additionally, we observe that the synthetic jets positioned at 105° (J_1^1 and J_2^1) exhibit a more pronounced transient response in both drag and lift coefficients, indicating a higher sensitivity to the jet actuation. This is a subtle but important observation that will be discussed further in subsequent sections.

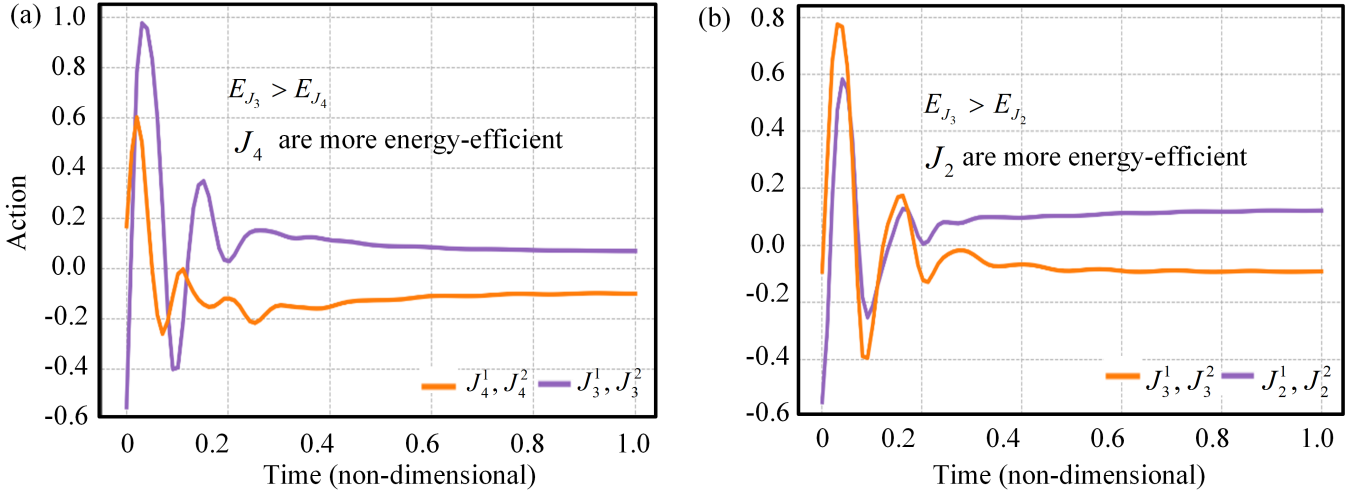


FIG. 12: Comparison of action values over non-dimensional time for different synthetic jets configurations around the cylinder. (a) Two pairs of jets: J_3^1, J_3^2 and J_4^1, J_4^2 . (b) Two pairs of jets: J_2^1, J_2^2 and J_3^1, J_3^2 .

2. Scenario B: Energy Consumption with Simultaneous Control (Two Pairs)

Flow control is executed using a strategy involving the mass flow rates of two pairs of synthetic jets referred to as Action in figure 12. The action values, representing the external energy consumed, are plotted over non-dimensional time for various jet configurations around the cylinder. Figure 12(a) depicts the control strategy utilizing two pairs of synthetic jets (J_3^1, J_3^2 and J_4^1, J_4^2). The initial peak in action values indicates the maximum energy required at the onset of the flow control process. As time progresses, the energy consumption stabilizes, suggesting that the control strategy becomes more consistent. The jet pair J_4^1, J_4^2 is observed to consume slightly less energy in the long run compared to J_3^1, J_3^2 , indicating that positioning synthetic jets at J_4 (75°) may offer an energy-saving advantage over positioning at J_3 (90°). The energy consumption for the control strategy utilizing two pairs of synthetic jets (J_3^1, J_3^2 and J_2^1, J_2^2) is shown in figure 12(b). The initial action peak is again prominent, reflecting the energy required at the start of the flow control process. Over time, both configurations exhibit reduced energy consumption, with action values stabilizing. However, jet pair J_3^1, J_3^2 demonstrates a slightly higher energy demand over time compared to J_2^1, J_2^2 , suggesting that J_2^1, J_2^2 may be more energy-efficient in maintaining effective flow control. This analysis provides a deeper understanding of the energy efficiency of different jet configurations in controlling flow around the cylinder. The initial peaks highlight the energy demands at the start, while the subsequent stabilization reflects the sustained maintenance of flow control. The differences in energy consumption among configurations can guide the selection of jet positions to optimize flow control efficiency, with the J_4 position (75°) and J_2 position (105°) showing potential as a more energy-efficient choice.

3. Scenario B: Energy Consumption with Simultaneous Control (Three Pairs)

A detailed analysis of energy consumption during flow control using three pairs of synthetic jets is presented in figure 13. These jets (J_2^1, J_2^2 , J_3^1, J_3^2 , and J_4^1, J_4^2) are symmetrically arranged around the cylinder at angular positions of 75° (J_4), 90° (J_3), and 105° (J_2) relative to the forward stagnation point (0°). The action values shown in figure 13 correspond to the external energy expenditure associated with jet operation over non-dimensional time. In this context, E_{J_3} denotes the external energy required by the synthetic jets pair J_3 , comprising J_3^1 and J_3^2 , to achieve effective flow control. Interestingly, when compared to figure 12, where only two pairs of synthetic jets are employed, figure 13 demonstrates that the activation of three pairs of synthetic jets leads to a reduction in the peak external energy demand for each individual jet. This suggests that the simultaneous use of additional jets can distribute the energy load more effectively, thereby enhancing the overall efficiency of the flow control strategy.

At the onset, the action values across all three configurations, as optimized via DRL, exhibit pronounced peaks. Following the initial transient phase, the energy consumption stabilizes across all configurations, indicating a uniform energy requirement as the flow control reaches a steady state. The jet pair positioned at 90° (J_3) demonstrates the highest peak, suggesting that the energy consumption at the 90° jet position (E_{J_3}) is significantly higher than that of the other two configurations ($E_{J_4} \approx E_{J_2}$). This observation implies that the 90° jet position demands greater energy to achieve comparable control efficacy, thereby indicating a lower energy efficiency compared to the 75° and 105° positions. The variations in energy consumption associated with different jet positions for flow control around a cylinder, emphasizing the critical importance of selecting an optimal jet position to

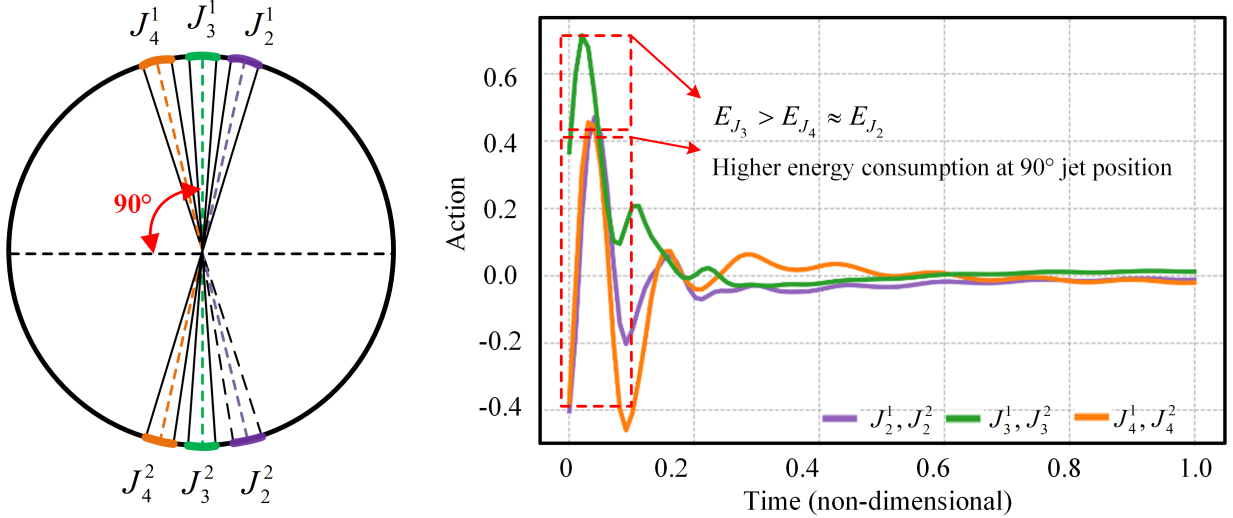


FIG. 13: Energy consumption analysis for different jet pairs positioned around a cylinder. The left image shows the jet pairs J_2 , J_3 , and J_4 , with azimuth angles ranging from 75° to 105° . The right image presents the corresponding actuation values of the synthetic jets over non-dimensional time for each jet configuration.

minimize energy consumption while maintaining effective flow regulation, are highlighted in figure 13. The results suggest that the jet positions at 75° (J_4) and 105° (J_2) exhibit similar and reduced energy demands, indicating their superiority in sustaining flow control. Conversely, although the 90° position is frequently utilized in flow control applications, it may not represent the most energy-efficient choice. These findings are vital for refining flow control strategies, particularly in scenarios where energy efficiency is of paramount importance.

IV. RESULTS: FLOW CONTROL PERFORMANCE OF A SQUARE CYLINDER

In this section, we use the flow around a square cylinder as the DRL training environment, employing the control capabilities of a PPO agent to implement active flow control through synthetic jets positioned near the front and rear corners of the cylinder. The flow around a square cylinder is characterized by earlier separation at sharp edges, more complex and turbulent wake structures, and greater flow instability compared to a circular cylinder, making it more challenging to control. This study aims to understand how the positioning of synthetic jets influences flow control performance and costs in this context. To explore these effects, we design four configurations with a single pair of synthetic jets, one configuration with two pairs of synthetic jets, and one additional configuration with a single pair of synthetic jets. These configurations are specifically designed to assess the impact of jet placement on the effectiveness and efficiency of flow control.

A. A pair of synthetic jets controllers

1. Scenario A: Control Performance of Jet Pair

DRL is used to develop flow control strategies for the flow around a square cylinder, as shown in figure 14. The figure provides a detailed analysis of the influence of synthetic jet positioning on flow control performance within the square geometry. The reward function serves as the primary metric for evaluating the effectiveness of the control strategies developed by the DRL agent. Initially, the reward values are low, reflecting the early stages of learning and the exploration of suboptimal strategies. As training progresses, a significant increase in the reward function is observed across all jet configurations, particularly between the 500th and 2000th episodes. This trend indicates that the DRL agent is successfully optimizing the control strategies, leading to improved flow control. The consistent rise in the reward function suggests that the DRL algorithm is steadily refining its policy, converging toward an optimal solution. The agent's ability to adapt and improve through continuous learning highlights the potential of DRL in addressing complex flow control challenges. The reward function behavior during DRL training is examined with synthetic jets positioned near the front and rear corners of a square cylinder, specifically for the configurations J_2^1, J_2^2 , J_3^1, J_3^2 , and J_4^1, J_4^2 , as illustrated in figure 14(a). The results indicate that the reward function exhibited the most rapid growth when

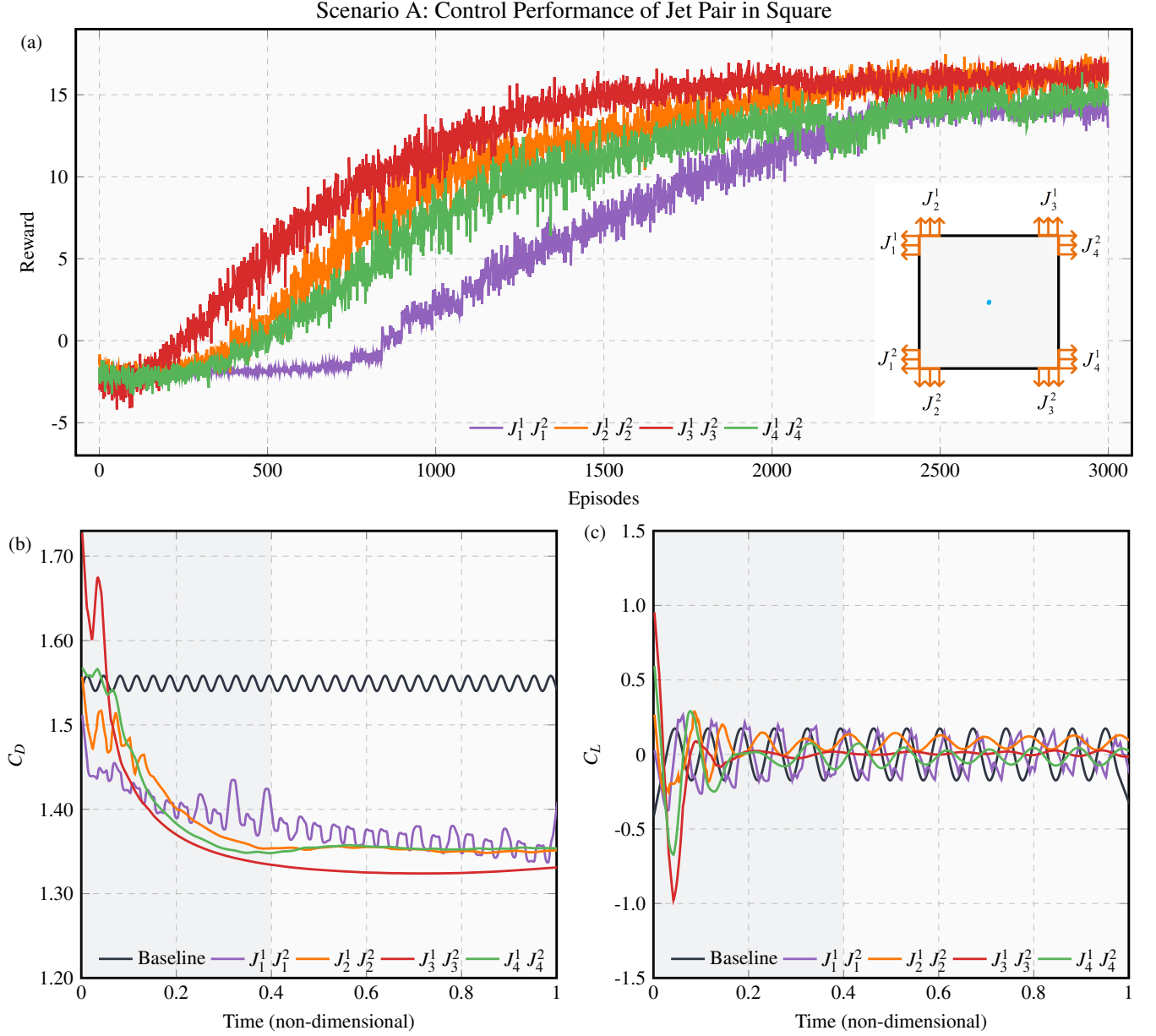


FIG. 14: Performance evaluation of different jet configurations for flow control around a square cylinder. (a) Reward curves over training episodes for various jet positions. (b) C_D over non-dimensional time, comparing the baseline scenario with different jets configurations. (c) C_L over non-dimensional time, comparing the baseline scenario.

the jets are positioned at J_3^1, J_3^2 , while the slowest growth was observed for the J_2^1, J_2^2 configuration. This variation in growth rates underscores the superior adaptability of the J_3^1, J_3^2 configuration, as it allows the DRL agent to more effectively achieve the control objectives. The accelerated increase in the reward function associated with J_3^1, J_3^2 indicates that this setup is intrinsically more aligned with the flow control requirements, facilitating a more efficient optimization process.

In contrast, the slower growth observed for J_2^1, J_2^2 suggests that this configuration may encounter challenges in interacting with the flow dynamics, potentially due to a more complex flow behavior that hinders the learning efficiency of the agent. These findings highlight the critical role of jet positioning in optimizing flow control strategies. The distinct differences in reward growth rates not only reflect the varying degrees of learning efficiency but also emphasize the importance of strategic jet placement in enhancing the performance of DRL-based flow control. Configurations like J_3^1, J_3^2 , which demonstrate rapid reward growth, are evidently more conducive to achieving efficient and precise flow manipulation, whereas slower growth configurations, such as

TABLE I: Control effectiveness and energy consumption analysis using a single pair of synthetic jets on a square cylinder.

Jet	$C_{D,Base}$	$C_{D,Mean}$	Reduction (%)	$C_{D,Std}$	$C_{L,Mean}$	$C_{L,Std}$	A_{Std}	A_{Mean}	Action ratio (%)
J_1	1.549	1.361	12.1	0.028	0.008	0.164	0.880	19.594	44.0
J_2	1.549	1.344	13.2	0.002	0.072	0.030	-0.506	0.177	25.3
J_3	1.549	1.326	14.4	0.002	0.008	0.013	-0.033	0.037	1.7
J_4	1.549	1.353	12.6	0.001	-0.012	0.043	0.184	0.654	9.2

J_2^1, J_2^2 , may require more refined strategies or adjustments to overcome inherent complexities. These insights are vital for refining jet configurations and advancing the effectiveness of DRL algorithms in complex fluid dynamics applications.

The relationship between the drag coefficient and non-dimensional time is presented for four different jet placement configurations, compared to the baseline case without active control, as shown in figure 14(b). The baseline curve, representing the drag coefficient without control, exhibits periodic oscillations. Once the synthetic jets are activated, the drag coefficient of the square cylinder decreases significantly across all configurations. The most notable reduction occurs when the jets are positioned near the rear corner points at J_3^1, J_3^2 , indicating this placement is the most effective for drag reduction. In contrast, jets placed near the front corners at J_1^1, J_1^2 show a clear reduction in drag, but with transient spikes and oscillations, suggesting a dynamic interaction between the jets and the flow. Configurations at J_2^1, J_2^2 and J_4^1, J_4^2 also result in substantial drag reduction, though less pronounced than at J_3^1, J_3^2 . This analysis highlights the critical role of jet placement in optimizing flow control and reducing aerodynamic drag around square cylinders.

The relationship between the lift coefficient and non-dimensional time is depicted for various synthetic jet configurations, compared to the baseline scenario, as shown in figure 14(c). The baseline lift coefficient exhibits periodic fluctuations throughout the time series, characteristic of the natural vortex shedding around the square cylinder. When the synthetic jets are positioned at $J_2^1, J_2^2, J_3^1, J_3^2$, and J_4^1, J_4^2 , a significant attenuation in the lift coefficient is observed. Specifically, the configuration at J_3^1, J_3^2 induces the most pronounced initial reduction in the lift coefficient, which rapidly stabilizes near zero, indicating effective suppression of the unsteady aerodynamic forces. Furthermore, the configurations at J_2^1, J_2^2 and J_4^1, J_4^2 lead to a marked reduction in both the amplitude and frequency of the lift coefficient oscillations, thereby significantly damping the lift fluctuations. This suggests a successful mitigation of vortex-induced forces through controlled jet actuation. However, when the jets are located at J_1^1, J_1^2 , the lift coefficient fails to exhibit a similar reduction. Instead, transient spikes and persistent oscillations are present, indicating that this jet configuration is less effective in altering the flow structures responsible for lift generation. These results crystallize the crucial role of optimal jet placement in flow control, where precise modulation of aerodynamic forces, such as lift, is essential for achieving effective performance. Jet configurations that interact favorably with the complex flow dynamics around the square cylinder are the most effective in stabilizing the flow and reducing oscillatory forces.

2. Scenario A: Energy Consumption of Jet Pair

The external energy consumed for flow control varies significantly with the positioning of the synthetic jets at $J_1^1, J_1^2, J_2^1, J_2^2, J_3^1, J_3^2$, and J_4^1, J_4^2 . The time evolution of energy consumption for these different configurations is illustrated in figure 15. When the jets are located at J_1^1, J_1^2 , the energy required for flow control is substantially higher, accompanied by pronounced fluctuations, indicating instability in mass flow rates. This instability suggests lower control efficiency due to complex interactions with the flow field, making it difficult to achieve consistent and effective flow manipulation. In contrast, when the jets are positioned at $J_2^1, J_2^2, J_3^1, J_3^2$, and J_4^1, J_4^2 , the control strategies exhibit more stable behavior, with minimal oscillations and near-zero values, reflecting efficient and balanced flow control with lower energy input. Notably, the J_3^1, J_3^2 configuration requires the least energy at the onset of control and remains the most stable over time. The comparison between the less stable J_1^1, J_1^2 configuration and the more stable configurations highlights the differences in energy efficiency and control stability. The larger and more unstable fluctuations observed with J_1^1, J_1^2 indicate lower energy efficiency and greater challenges in maintaining flow control. In contrast, J_3^1, J_3^2 demonstrates more predictable and controlled energy usage, effectively sustaining flow control with lower energy costs.

The activation states of the synthetic jets at positions J_1, J_2, J_3 , and J_4 , along with the velocity contours of the flow field after flow control is completed, are depicted in figure 16. The velocity contours show that when the jets are positioned near the rear sides of the square cylinder at J_3 , vortex shedding in the wake is fully suppressed. At J_4 , located on the rear face of the cylinder, the recirculation region expands significantly compared to the initial stages of control. When the jets are placed closer to the upstream at J_2 , periodic actuation of the synthetic jets enhances the flow stability around the cylinder. Finally, at J_1 , positioned at the front of the cylinder, the interaction between the synthetic jets and the free stream improves flow stability, although alternating vortex shedding still persists.

The control performance and energy consumption of flow control based on DRL are summarized in table I. The control performance is evaluated by the percentage reduction in $C_{D,Mean}$ relative to $C_{D,Base}$, the standard deviation of $C_{D,Std}$ for controlled

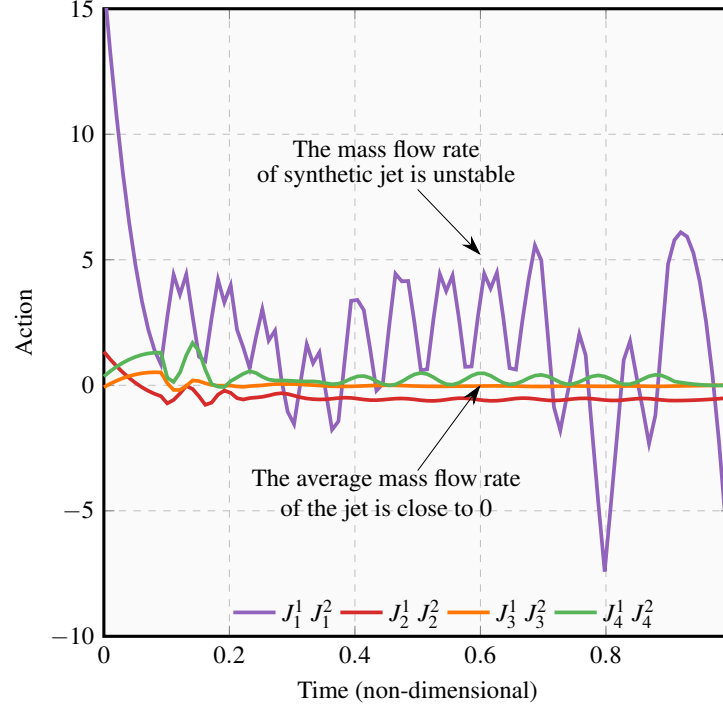


FIG. 15: Energy consumption over non-dimensional time for jet pairs positioned at various locations around the square cylinder. The jet pair locations include: $J_1^1, J_1^2, J_2^1, J_2^2, J_3^1, J_3^2$, and J_4^1, J_4^2 .

flow, and the mean ($C_{L,Mean}$) and standard deviation ($C_{L,Std}$) of the lift coefficient. The energy consumption for flow control is quantified by the mean (A_{Mean}) and standard deviation (A_{Std}) of the jet actuation magnitude, as well as the action ratio (%) of the average jet flow rate to the upstream inlet flow rate. The quantified control performance and energy consumption metrics in the table indicate that positioning the synthetic jet at J_3 achieves the highest drag reduction efficiency of 14.4% using only 1.7% of the inlet flow rate, while minimizing the standard deviations of the C_D , C_L , and jet actuation. In contrast, placing the jet at J_1 requires 44% of the inlet flow rate to achieve a drag reduction of only 12.1%, with the highest standard deviations in C_D , C_L , and jet actuation, indicating the least stability.

Overall, the control performance of the jets varies significantly with placement. When the synthetic jets are positioned near the front corner points, vortex shedding is not fully suppressed due to the large separated flow reattaching along the sides of the square cylinder before separating again near the rear corners. In contrast, placing the jets near the rear corner points at position J_3 provides more effective flow control, leading to the complete suppression of vortex shedding. [Chen et al.](#) used DRL-based flow control to reduce vortex-induced vibrations around a square cylinder ($Re = 100$) and compared the control effects of jet placement at the front, middle, and rear positions along the cylinder's side. Their results showed that full suppression was achieved only near the rear corners, consistent with our findings [47].

B. Multiple pairs of synthetic jets controllers

1. Scenario B: Control Performance of Multiple Jets Control

Additional experiments are designed to implement flow control using multiple pairs of synthetic jets simultaneously. The results of DRL training and its impact on flow control for a square cylinder with various jet configurations are illustrated in figure 17. For comparison, results using a single pair of synthetic jets are also provided. The evolution of the reward functions during training for different jet configurations is shown in figure 17(a). The reward function serves as a critical metric for evaluating the effectiveness of the DRL agent in optimizing flow control strategies. In this figure, $J_2^1 J_2^2$, $J_3^1 J_3^2$, and $J_4^1 J_4^2$ represent specific jet positions on the square cylinder.

Across all four configurations, the reward functions increase as training progresses, indicating that the DRL agent is successfully learning and refining the flow control strategies. Initially, the reward values are low, reflecting the early stages of learning when the agent explores various control strategies. As the number of episodes increases, the reward function for each jet configuration shows steady improvement, particularly between 500 and 2000 episodes. The gradual rise in the reward values suggests that the

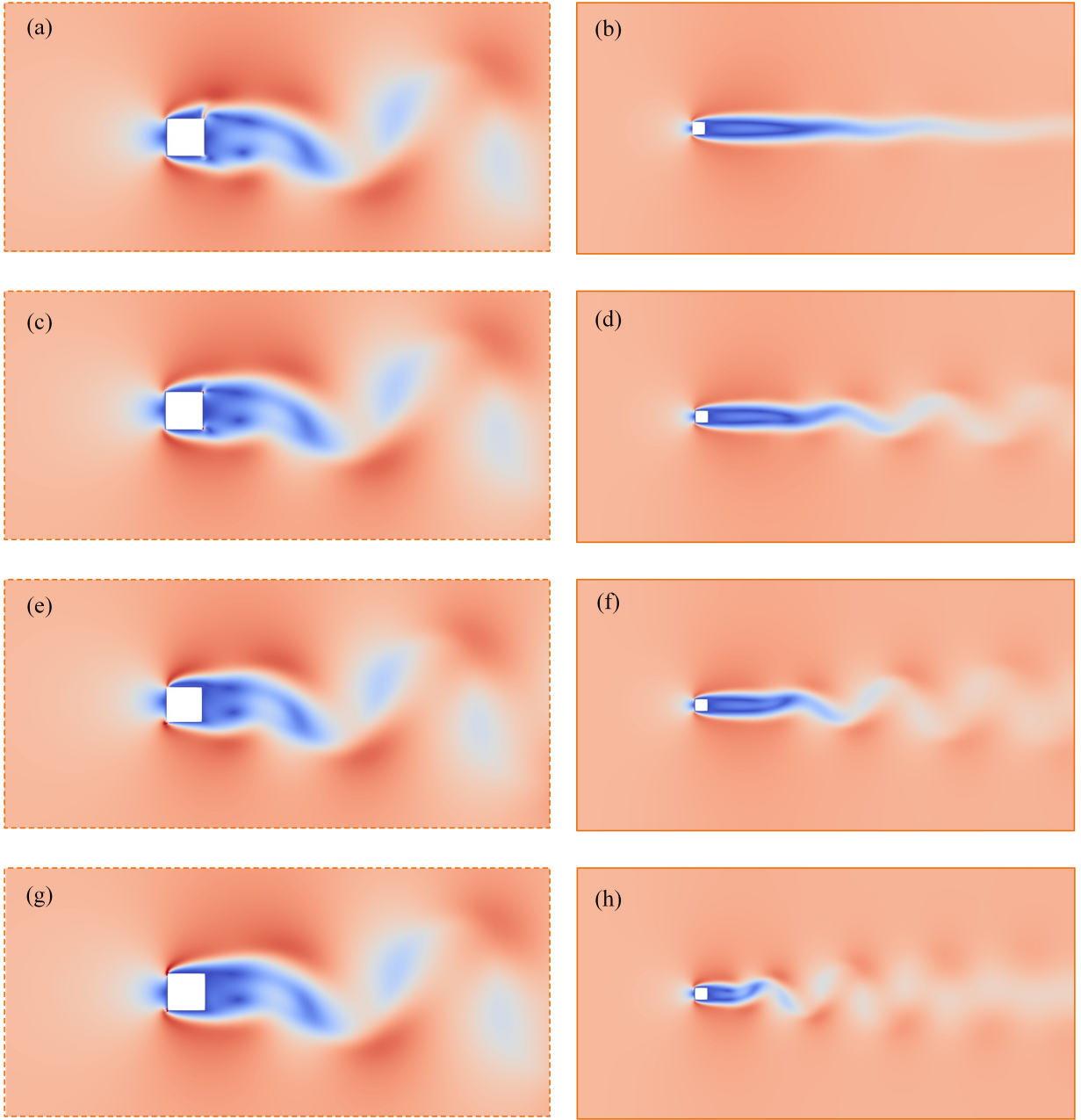


FIG. 16: Velocity contours of flow around a square cylinder with synthetic jets positioned at various locations. The left column shows the flow with active jet control, while the right column presents the corresponding flow control results. (a) and (b) Jets J_3^1 and J_3^2 on the top and bottom sides near the rear corners. (c) and (d) Jets J_4^1 and J_4^2 on the rear side. (e) and (f) Jets J_2^1 and J_2^2 on the top and bottom sides near the front corners. (g) and (h) Jets J_1^1 and J_1^2 on the front side.

DRL algorithm is progressively enhancing its strategy, leading to improved control performance. Notably, the reward function for the $J_3^1 J_3^2$ configuration exhibits faster growth, indicating that this setup is particularly effective in achieving the control objectives. The quicker convergence suggests that the agent is learning the optimal control strategy more efficiently with this configuration. Conversely, the more gradual increase in reward functions observed when using multiple pairs of synthetic jets suggests a more incremental learning process. The slower convergence may result from increased complexity in the fluid dynamics or suboptimal jet placement for these specific control tasks.

As a function of non-dimensional time for various jet configurations, compared to a baseline scenario without active flow control, the drag coefficient is illustrated in figure 17(b). The baseline drag coefficient exhibits periodic oscillations, a typical characteristic of unsteady flow around a square cylinder without control. Upon activating the synthetic jets, the drag coefficient

Scenario B: Control Performance of Multiple Jets Control in Square

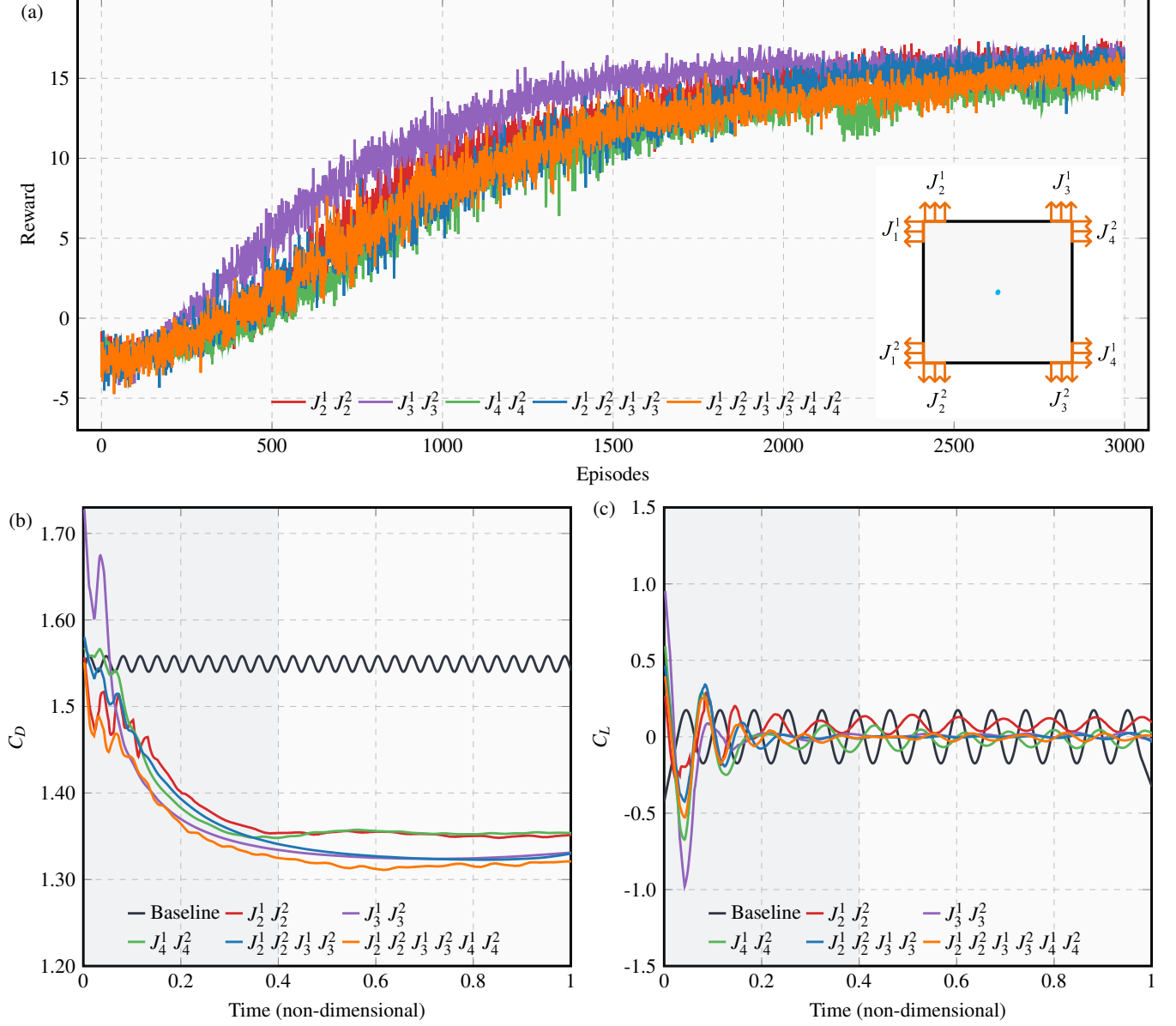


FIG. 17: Evaluation of flow control performance for a square cylinder using single and multiple synthetic jets configurations. (a) Reward curves during the training process for different jet placement configurations. (b) Drag coefficient (C_D) as a function of non-dimensional time for baseline and controlled flows. (c) Lift coefficient (C_L) as a function of non-dimensional time for baseline and controlled flows.

for all configurations decreases significantly, indicating the effectiveness of the control strategies. Specifically, the drag reduction achieved by single jet pairs positioned at J_2^1, J_2^2 and J_4^1, J_4^2 is less pronounced than that of the jet pair at J_3^1, J_3^2 . When both J_2^1, J_2^2 and J_3^1, J_3^2 are activated simultaneously, the drag reduction is almost identical to that achieved by J_3^1, J_3^2 alone, suggesting that adding the second jet pair (J_2^1, J_2^2) does not provide additional benefit. However, when all three jet pairs (J_2^1, J_2^2 , J_3^1, J_3^2 , and J_4^1, J_4^2) are activated together, there is a more substantial reduction in drag compared to both the single jet pair (J_3^1, J_3^2) and the two jet pairs (J_2^1, J_2^2 and J_3^1, J_3^2). This enhanced drag reduction comes at the cost of some stability, reflecting the more complex interactions involved in controlling the flow with multiple jet pairs. This analysis highlights the trade-offs between achieving greater drag reduction and maintaining stability when using multiple synthetic jets in flow control. The results suggest that while adding more jets can further reduce drag, it may also introduce additional challenges in maintaining a stable control strategy.

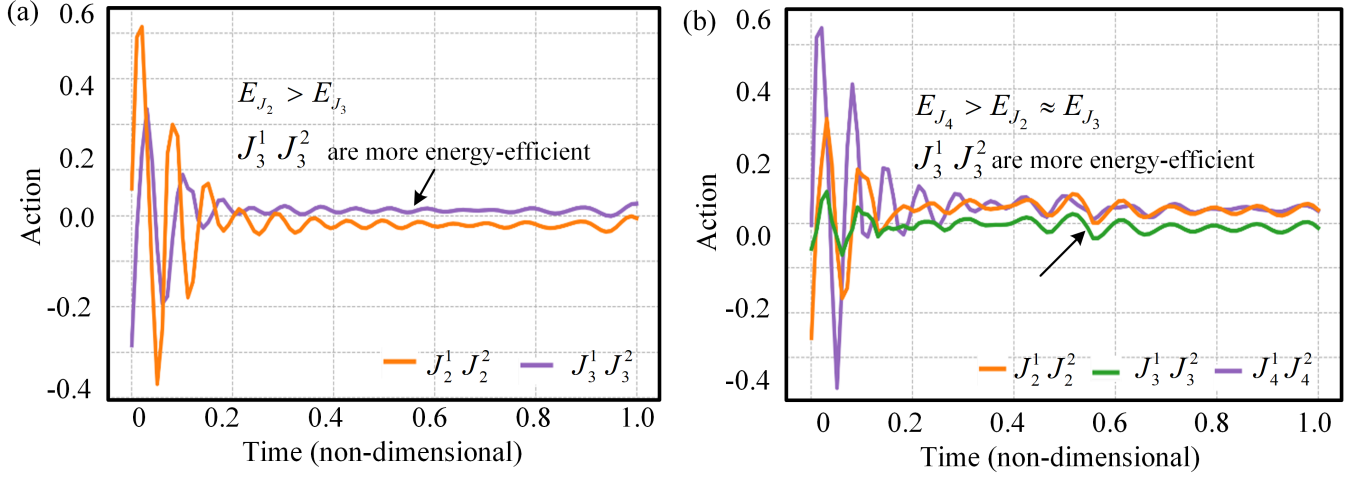


FIG. 18: Comparison of energy consumption during flow control using different synthetic jets configurations around a square cylinder. (a) Energy consumption with two jet pairs J_2^1, J_2^2 and J_3^1, J_3^2 . (b) Energy consumption with three jet pairs $J_2^1, J_2^2, J_3^1, J_3^2$, and J_4^1, J_4^2 .

Over non-dimensional time for various jet configurations, compared to a baseline scenario without active control, the lift coefficient is illustrated in figure 17(c). The baseline C_L without control exhibits periodic oscillations. The activation of synthetic jets significantly reduces both the amplitude and frequency of these oscillations, stabilizing the lift coefficient closer to zero or the desired level. This suppression of lift fluctuations helps create a more stable flow field by mitigating the unsteady forces acting on the cylinder. Specifically, the configuration with jets positioned at J_3^1, J_3^2 shows a more pronounced reduction in lift compared to those at J_2^1, J_2^2 or J_4^1, J_4^2 . When two jet pairs (J_2^1, J_2^2 and J_3^1, J_3^2) are activated simultaneously, the reduction in lift is similar to that achieved with J_3^1, J_3^2 alone, indicating that the additional jet pair does not significantly enhance control. When all three pairs of jets ($J_2^1, J_2^2, J_3^1, J_3^2$, and J_4^1, J_4^2) are activated simultaneously, the oscillations in the lift coefficient become more pronounced, indicating increased flow instability. While activating all three jet pairs enhances drag reduction, it also introduces additional instability in the lift coefficient. This analysis demonstrates that the J_3^1, J_3^2 configuration provides the most efficient and effective flow control, as evidenced by rapid reward function convergence, significant drag reduction, and stabilized lift. Although the simultaneous activation of two jet pairs (J_2^1, J_2^2 and J_3^1, J_3^2) yields similar control performance, it does not achieve the same level of convergence efficiency as using J_3^1, J_3^2 alone. The activation of all three jet pairs, while improving drag reduction, leads to increased flow instability, which will be further analyzed in the next section in relation to the energy consumption required for flow control.

2. Scenario B: Energy Consumption with Simultaneous Control (Two Pairs and Three Pairs)

The external energy consumption over non-dimensional time for flow control with two (a) and three (b) synthetic jets pairs around a square cylinder is depicted in figure 18. When comparing the single-pair synthetic jets control in figure 15 to the multi-pair configuration in figure 18, it is evident that the energy consumption in the multi-jet scenario is reduced by an order of magnitude relative to the single-jet case. Where two pairs of synthetic jets, J_2^1, J_2^2 and J_3^1, J_3^2 , are simultaneously employed, significant peaks in action values for both configurations are shown in the initial phase in figure 18(a), indicating a high energy demand at the onset of flow control. This peak reflects the system response to the abrupt introduction of control forces generated by the jets. As time progresses, the action values stabilize, signifying that the energy required to maintain control has reached a steady state. Notably, the energy demand for the jets positioned at J_3^1, J_3^2 consistently remains lower than that for J_2^1, J_2^2 , highlighting the greater energy efficiency of the J_3 configuration. The sustained lower action values suggest that this configuration achieves the desired flow control with less external energy input, making it a more efficient option for long-term operation.

The control performance is illustrated in figure 18(b) when three pairs of jets ($J_2^1, J_2^2, J_3^1, J_3^2$, and J_4^1, J_4^2) are employed simultaneously. The action values indicate the energy efficiency of various jet configurations in controlling the flow around the square cylinder, with lower sustained values signifying more energy-efficient setups. Similar to the two-jet configuration, the three-jet setup also exhibits peak action values during the initial phase of control, indicative of the high initial energy demand required to establish effective control. As the system stabilizes, the action values across all jet pairs settle into a steady state.

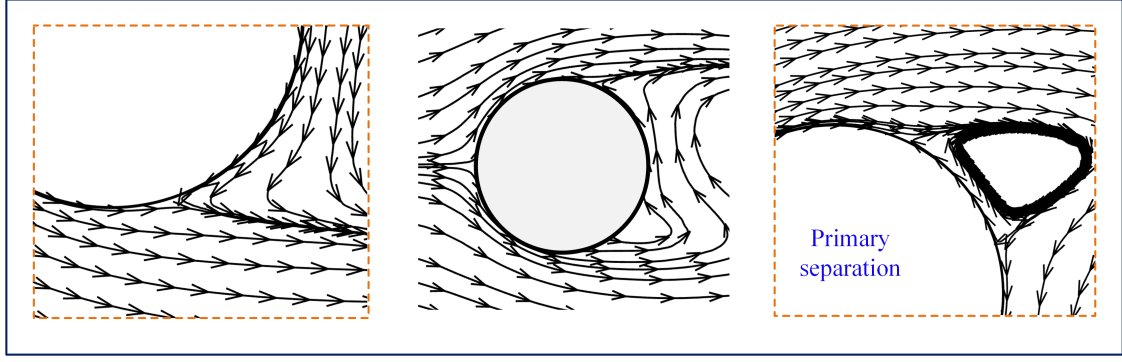
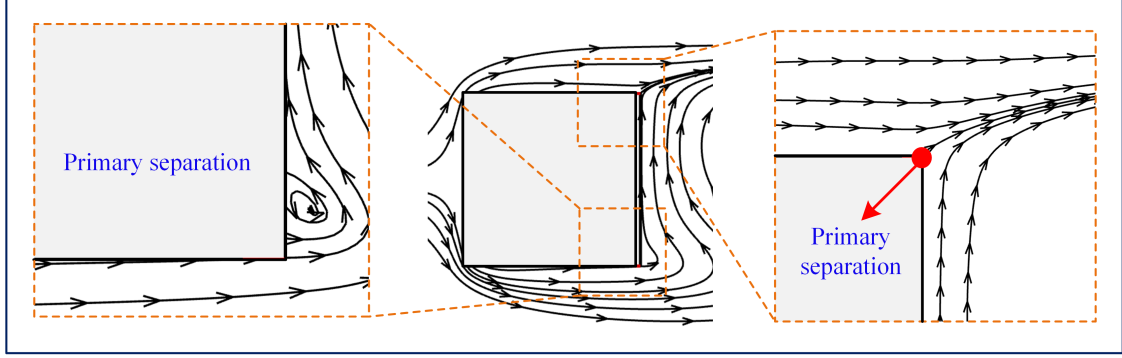
(a) $Re = 100$, baseline streamline(a) $Re = 100$, baseline streamline

FIG. 19: (a) Streamline pattern for the baseline flow at $Re = 100$ around a circular cylinder. (b) Streamline pattern for the baseline flow at $Re = 100$ around a square cylinder.

Among the three-jet configurations, the jets positioned at J_4^1, J_4^2 demonstrate the highest sustained action values, indicating a higher energy requirement to maintain effective flow control. In contrast, the jets at J_3^1, J_3^2 consistently show lower energy consumption compared to those at J_4^1, J_4^2 and J_2^1, J_2^2 , reinforcing their observed efficiency in the two-jet scenario. The J_3^1, J_3^2 configuration emerges as the most energy-efficient across both two-jet and three-jet configurations, suggesting that the jets positioned at J_3 (likely near critical flow regions such as separation points) provide effective control while minimizing energy consumption. This finding aligns with conclusions drawn from single-jet scenarios, where jets at J_3 consistently maintain control with minimal energy input, favoring long-term operational efficiency. The analysis underscores the importance of strategic jet placement in optimizing flow control performance while minimizing energy expenditure. The consistent performance of the J_3 jets highlights their role as the optimal balance between control effectiveness and energy efficiency.

V. DISCUSSION: THE PHYSICAL INSIGHT OF FLOW CONTROL STRATEGY

A. Flow separation phenomenon

§ section III and § section IV provide a detailed examination of the effects of various jet configurations on flow control performance. To further analyze the underlying mechanisms of flow control in relation to fluid dynamics, we present a comprehensive discussion of the control performance for both circular and square cylinder flows. When $Re = 100$, the flow around the circular cylinder exhibits a stable laminar characteristic with well-defined separation points, as shown in figure 19. Flow separation occurs symmetrically on both sides of the cylinder, approximately 105° from the forward stagnation point. At this location, the adverse pressure gradient causes the boundary layer to detach from the surface, marking the onset of flow separation. This detachment initiates the formation of a wake behind the cylinder, where alternating vortices periodically shed, ultimately leading to the development of the characteristic von Kármán vortex street downstream.

In contrast, for a square cylinder at the same Reynolds number, the sharp changes in geometry result in flow separation occurring at the four sharp corners of the body. The boundary layer detaches immediately at these edges, forming distinct

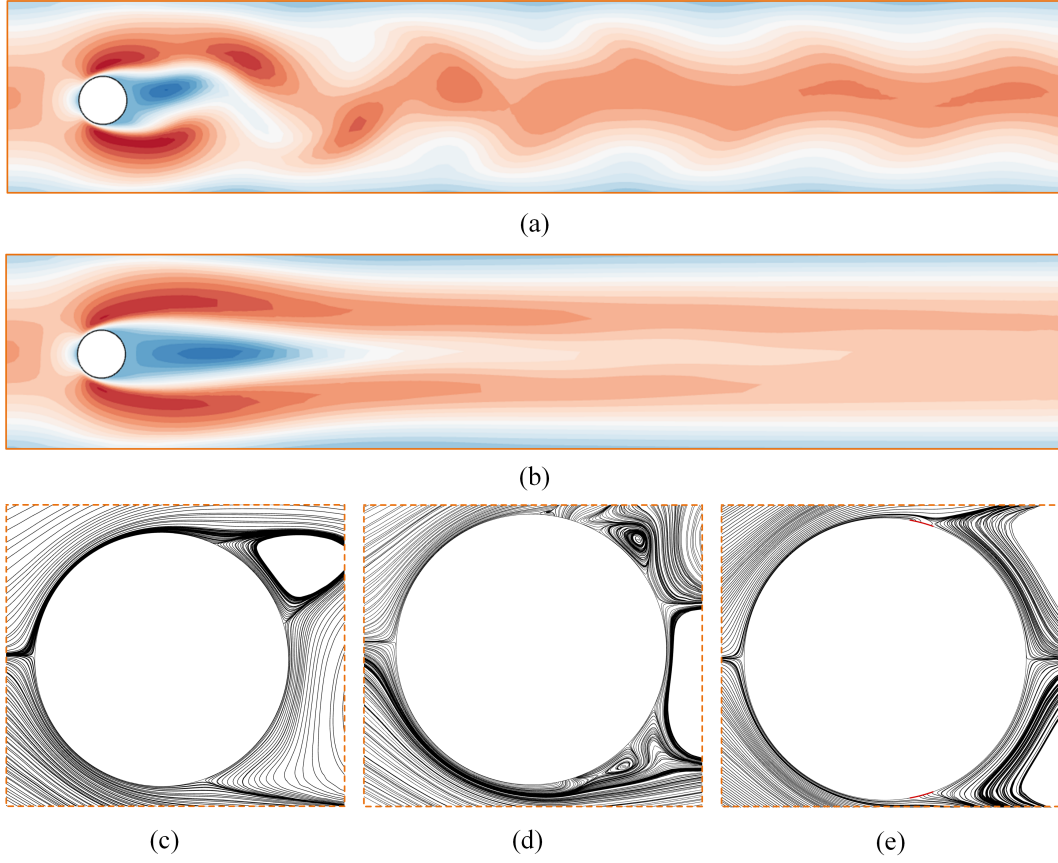


FIG. 20: (a) Velocity contours of flow around a cylinder in the baseline case. (b) Velocity contours of the controlled flow with synthetic jets positioned at a 105° azimuthal angle. (c) Streamlines around the cylinder in the baseline case. (d) Streamlines around the cylinder with active synthetic jets at a 105° azimuthal angle. (e) Streamlines around the cylinder after flow control is completed with synthetic jets activated at a 105° azimuthal angle.

vortices. Especially, large separation bubbles form near the rear corners, creating a pronounced separation zone in the wake. The differing nature of flow separation around circular and square cylinders necessitates distinct control strategies, posing unique challenges when applying reinforcement learning algorithms for flow control.

B. Flow control mechanism

Through comparative analysis, the optimal position for synthetic jets around a circular cylinder is found to be at a 105° angle from the front stagnation point. At this position, drag and lift are significantly reduced, vortex shedding is fully suppressed, and energy consumption is minimized. This result aligns with the findings of [27] at $Re = 100$, which demonstrated superior control performance using a sensor at 105° . The results further confirm that the 105° configuration offers the best balance between energy efficiency and flow stability, as detailed in § III. In figure 20, the flow control effectiveness of the synthetic jets positioned at 105° (J_2^1 and J_2^2) is illustrated, showcasing flow streamlines at three distinct time points—before, during, and after control activation. figure 20 (a) shows the baseline flow with the typical Kármán vortex street downstream of the cylinder. After activating the synthetic jets at 105° , the recirculation region on the cylinder's rear side expands, and vortex shedding is entirely suppressed, as depicted in figure 20 (b). And, figure 20 (c) reveals the flow separation region and the formation of a large, closed vortex on the rear side of the cylinder in baseline flow.

When the jet positioned at the 105° azimuth is activated, it operates through alternating ejection and suction of the surrounding fluid, effectively altering the local flow without introducing any new mass into the system, as shown in figure 20 (d). The synthetic jets located at J_2^1 and J_2^2 consistently satisfy the condition $Q_1 + Q_2 = 0$, ensuring that the net mass flow in the system remains zero. However, the momentum and hydrodynamic impulse generated by the jets are not zero. The interaction between the synthetic jets and the crossflow leads to the formation of new vortex pairs. These high-energy vortices convect over the cylinder, locally modifying the streamlines around its surface. As a result, the apparent aerodynamic shape of the cylinder is

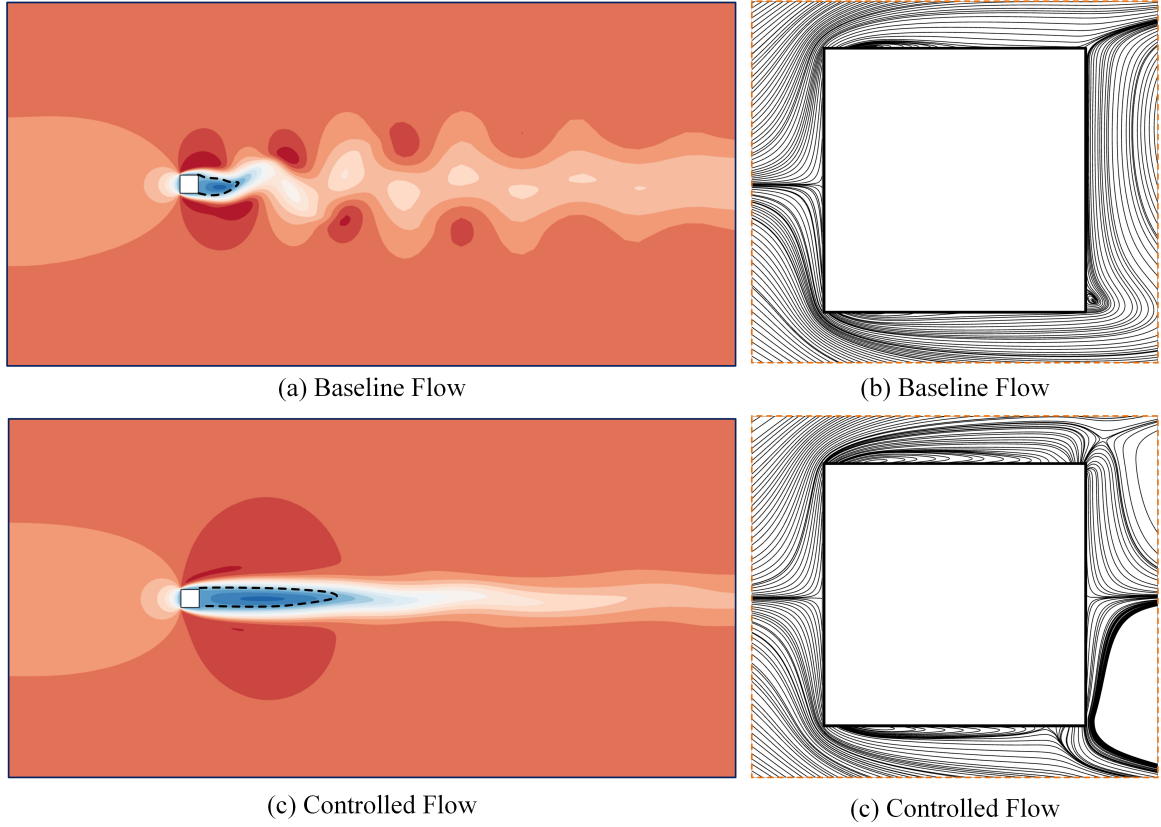


FIG. 21: (a) Velocity contours of flow around a square cylinder in the baseline case. (b) Streamlines around the square cylinder in the baseline. (c) Velocity contours of the controlled flow with jets positioned at the J_3 location. (d) Streamlines around the square cylinder after flow control with jets positioned at the J_3 location.

significantly improved, along with its aerodynamic characteristics. By altering the local streamlines and inducing noticeable surface modifications, synthetic jets effectively control the flow, reducing drag and improving overall aerodynamic efficiency. [73] and [74] experimentally demonstrated the formation, evolution, and control mechanisms of synthetic jets in flow control. The use of a DRL-based approach reveals a dynamically evolving flow control process that aligns with their findings. This consistency further validates the effectiveness of synthetic jets in altering flow behavior and enhancing aerodynamic performance through active flow control strategies.

In § IV, the training results for various jet configurations around the square cylinder demonstrate that positioning synthetic jets near the rear corners of the cylinder yields the optimal control performance, achieving both low energy consumption and high flow control efficiency. In this configuration, drag reduction and lift suppression are significantly enhanced, while vortex shedding in the wake is entirely suppressed with minimal external energy input. Further analysis of the separation points for both square and circular cylinders, as shown in figure 19, combined with the results from § III and § IV, indicates that placing synthetic jets near the flow separation points is critical for effective flow control. Only when the jets are positioned in close proximity to these separation points can vortex shedding be fully suppressed. The comparison between the baseline flow and the controlled flow, with jets positioned at the rear corners (J_3^1 and J_3^2), is illustrated in figure 21. The placement of the synthetic jets near the rear corners effectively suppresses vortex formation and stabilizes the wake flow. Streamline patterns around the square cylinder reveal significant local alterations near the rear corners due to the action of the synthetic jets. In the controlled flow, the flow separation regions on both sides of the square cylinder become more defined, and two stable, closed separation bubbles form on the cylinder's rear face. The interaction between synthetic jets and the external flow induces significant changes in local flow patterns and streamlines, facilitating linear momentum transfer without mass addition. The alternating phases of blowing and suction generate vortices that enhance boundary layer mixing, supplying the necessary energy to overcome adverse pressure gradients and enabling complete flow reattachment around the square cylinder.

VI. CONCLUSIONS

We employ DRL algorithms to train synthetic jet-based flow control strategies for circular and square cylinders. The DRL training process involves the DRL agent learning to manipulate the jets by interacting with the dynamic flow environment, refining its control policy through iterative adjustments to minimize drag and suppress flow instabilities. The overarching goal is to determine the optimal jet placement that balances energy efficiency and flow control effectiveness, addressing the inherent complexities of achieving effective control while minimizing energy expenditure. To this end, we systematically investigate a range of jet configurations, encompassing both single-jet and multi-jet control strategies, to comprehensively evaluate their influence on flow characteristics and energy consumption. The main findings include the identification of the optimal jet placement for circular and square cylinders, as well as qualitative guidelines derived from detailed hydrodynamic analyses.

1. Flow around a circular cylinder scenario. The single-jet training results show that positions J_1 (120°) and J_5 (60°) exhibit slower and lower convergence of the reward function, indicating lower training effectiveness. In contrast, positions J_2 , J_3 , and J_4 converge rapidly, suggesting superior control strategy acquisition. Although all five positions achieve an 8% drag reduction and 99% lift coefficient suppression, J_1 and J_5 require three times the energy of position J_2 (at 105°) to reach the same performance level. The J_1 (120°) and J_5 (60°) positions show poor convergence and energy efficiency, J_1 and J_5 are less favorable for optimizing flow control strategies. When training the agent to control multiple pairs of synthetic jets, multi-actuator control does not demonstrate significant advantages in convergence or drag reduction performance compared to single-actuator control. In fact, multi-actuator control exhibits delayed convergence and reduced flow stability. However, simultaneous multi-actuator control effectively reduces initial energy consumption. When two pairs of synthetic jets are activated, J_4 (75°) and J_2 (105°) consume less energy compared to J_3 (90°). For cases with three pairs of jets activated simultaneously, the initial energy consumption is lower than that of single- or two-jet configurations, and J_2 (105°) provides better stability than J_4 (75°).
2. Flow around a square cylinder scenario. When trained to control a single pair of synthetic jets, the agent performs best with jets at J_3 , showing superior convergence, stability, and control performance compared to J_1 , J_2 , and J_4 . Jets at J_3 achieve superior control, with 14.4% drag reduction using only 1.7% of the inlet flow rate, demonstrating minimal energy consumption and high stability. In contrast, jets at J_1 require 44% of the flow rate for only 12.1% drag reduction, resulting in higher energy consumption and lower stability. The use of dual jet pairs at J_2 and J_3 leads to a substantial reduction and stabilization of drag and lift coefficients, achieving control performance comparable to that of a single jet pair positioned at J_3 . However, the reward function for the single jet pair at J_3 shows faster convergence and greater stability compared to using two jet pairs, indicating higher control efficiency. When all three jet pairs (J_2 , J_3 , and J_4) are used simultaneously, the jets at J_3 achieve effective flow control with minimal energy consumption. These findings suggest that the jets at J_3 offer the best performance in terms of both control effectiveness and energy efficiency.
3. The DRL training results indicate that positioning synthetic jets at approximately 105° from the front stagnation point on a circular cylinder and near the rear corners of a square cylinder yields the best energy efficiency and flow control performance. When synthetic jets are strategically placed at the flow separation points, their interaction with the external flow significantly alters local flow patterns and streamlines, enhancing momentum transfer without mass addition and generating vortices that promote boundary layer mixing and complete flow reattachment. This placement not only optimizes flow control effectiveness but also minimizes energy consumption, highlighting the critical role of aligning synthetic jet positioning with key flow dynamics to achieve superior flow control performance, stability, and efficiency.

The applicability of DRL algorithms to flow control problems stems from their capability to autonomously learn optimal control strategies by interacting with complex, nonlinear flow environments. Through iterative training, DRL agents adaptively respond to evolving flow dynamics, making them a powerful tool for solving complex flow control challenges beyond the reach of conventional methods. Moreover, DRL's ability to capture complex state-action relationships enables it to explore a wider range of control strategies compared to traditional optimization methods. This study demonstrates that, through the strategic selection and placement of synthetic jets, an optimal balance between energy efficiency and control efficacy can be achieved. This balance is particularly evident when multiple jets are coordinated to enhance the overall flow control performance, as the synergistic interactions between jets lead to more pronounced control effects. The results highlight the critical importance of optimal jet placement in achieving superior control outcomes while simultaneously minimizing energy consumption, thereby providing a robust framework for energy-efficient flow control.

-
- [1] S. S. Collis and R. D. Joslin, Issues in active flow control: theory, control, simulation, and experiment, *Progress in aerospace sciences* **40**, 237 (2004).
 - [2] L. N. Cattafesta and M. Sheplak, Actuators for active flow control, *Annual Review of Fluid Mechanics* **43**, 247 (2011).
 - [3] T. R. Bewley, Flow control: new challenges for a new renaissance, *Progress in Aerospace Sciences* **37**, 21 (2001).
 - [4] M. Gad-el Hak, Modern developments in flow control, *Applied Mechanics Reviews* **49**, 365 (1996).
 - [5] S. L. Brunton, B. R. Noack, and P. Koumoutsakos, Machine learning for fluid mechanics, *Annual Review of Fluid Mechanics* **52**, 477 (2020).
 - [6] S. L. Brunton and B. R. Noack, Closed-Loop Turbulence Control: Progress and Challenges, *Applied Mechanics Reviews* **67**, 050801 (2015).
 - [7] L. P. Kaelbling, M. L. Littman, and A. W. Moore, Reinforcement learning: A survey, *Journal of artificial intelligence research* **4**, 237 (1996).
 - [8] K. Arulkumaran, M. P. Deisenroth, M. Brundage, and A. A. Bharath, Deep reinforcement learning: A brief survey, *IEEE Signal Processing Magazine* **34**, 26 (2017).
 - [9] C. Janiesch, P. Zschech, and K. Heinrich, Machine learning and deep learning, *Electronic Markets* **31**, 685 (2021).
 - [10] V. François-Lavet, P. Henderson, R. Islam, M. G. Bellemare, J. Pineau, *et al.*, An introduction to deep reinforcement learning, *Foundations and Trends® in Machine Learning* **11**, 219 (2018).
 - [11] V. Mnih, Playing atari with deep reinforcement learning (2013), arXiv preprint arXiv:1312.5602, [arXiv:1312.5602 \[cs.LG\]](#).
 - [12] J. Schulman, F. Wolski, P. Dhariwal, A. Radford, and O. Klimov, *Proximal policy optimization algorithms* (2017), [arXiv:1707.06347 \[cs.LG\]](#).
 - [13] R. S. Sutton and A. G. Barto, *Reinforcement Learning: An Introduction*, 2nd ed. (MIT Press, Cambridge, MA, 2018).
 - [14] E. Liang, R. Liaw, R. Nishihara, P. Moritz, R. Fox, K. Goldberg, J. Gonzalez, M. Jordan, and I. Stoica, RLLib: Abstractions for distributed reinforcement learning, in *Proceedings of the 35th International Conference on Machine Learning*, Proceedings of Machine Learning Research, Vol. 80, edited by J. Dy and A. Krause (PMLR, 2018) pp. 3053–3062.
 - [15] Y. Li, *Deep reinforcement learning: An overview* (2018), [arXiv:1701.07274 \[cs.LG\]](#).
 - [16] D. Silver, T. Hubert, J. Schrittwieser, I. Antonoglou, M. Lai, A. Guez, M. Lanctot, L. Sifre, D. Kumaran, T. Graepel, T. Lillicrap, K. Simonyan, and D. Hassabis, A general reinforcement learning algorithm that masters chess, shogi, and go through self-play, *Science* **362**, 1140 (2018).
 - [17] J. Rabault, F. Ren, W. Zhang, H. Tang, and H. Xu, Deep reinforcement learning in fluid mechanics: A promising method for both active flow control and shape optimization, *Journal of Hydrodynamics* **32**, 234 (2020).
 - [18] J. Viquerat, P. Meliga, A. Larcher, and E. Hachem, A review on deep reinforcement learning for fluid mechanics: An update, *Physics of Fluids* **34**, [10.1063/5.0128446](#) (2022).
 - [19] C. Vignon, J. Rabault, and R. Vinuesa, Recent advances in applying deep reinforcement learning for flow control: Perspectives and future directions, *Physics of Fluids* **35**, 031301 (2023).
 - [20] G. Novati, H. L. de Laroussilhe, and P. Koumoutsakos, Automating turbulence modelling by multi-agent reinforcement learning, *Nature Machine Intelligence* **3**, 87 (2021).
 - [21] M. Kurz, P. Offenhäuser, and A. Beck, Deep reinforcement learning for turbulence modeling in large eddy simulations, *International Journal of Heat and Fluid Flow* **99**, 109094 (2023).
 - [22] J. Viquerat, J. Rabault, A. Kuhnle, H. Ghraieb, A. Larcher, and E. Hachem, Direct shape optimization through deep reinforcement learning, *Journal of Computational Physics* **428**, 110080 (2021).
 - [23] J. Rabault, M. Kuchta, A. Jensen, U. Réglade, and N. Cerardi, Artificial neural networks trained through deep reinforcement learning discover control strategies for active flow control, *Journal of fluid mechanics* **865**, 281 (2019).
 - [24] H. Tang, J. Rabault, A. Kuhnle, Y. Wang, and T. Wang, Robust active flow control over a range of Reynolds numbers using an artificial neural network trained through deep reinforcement learning, *Physics of Fluids* **32**, 053605 (2020).
 - [25] J. Wang and H. Xu, Robust and adaptive deep reinforcement learning for enhancing flow control around a square cylinder with varying reynolds numbers, *Physics of Fluids* **36**, 054103 (2024).
 - [26] F. Ren, J. Rabault, and H. Tang, Applying deep reinforcement learning to active flow control in turbulent conditions, *Physics of Fluids* **33**, 037121 (2021), [2006.10683 \[physics\]](#).
 - [27] Q. Wang, L. Yan, G. Hu, W. Chen, J. Rabault, and B. Noack, Dynamic feature-based deep reinforcement learning for flow control of circular cylinder with sparse surface pressure sensing, *Journal of Fluid Mechanics* **988**, A4 (2024).
 - [28] H. Feng, Y. Wang, H. Xiang, Z. Jin, and D. Fan, How to control hydrodynamic force on fluidic pinball via deep reinforcement learning, *Physics of Fluids* **35**, 045137 (2023).
 - [29] Y.-Z. Wang, Y.-F. Mei, N. Aubry, Z. Chen, P. Wu, and W.-T. Wu, Deep reinforcement learning based synthetic jet control on disturbed flow over airfoil, *Physics of Fluids* **34**, 033606 (2022).
 - [30] J. Wang and H. Xu, Deep reinforcement learning-based active flow control of an elliptical cylinder: Transitioning from an elliptical cylinder to a circular cylinder and a flat plate, *Physics of Fluids* **36**, 074117 (2024).
 - [31] J. Li and M. Zhang, Reinforcement-learning-based control of confined cylinder wakes with stability analyses, *Journal of Fluid Mechanics* **932**, A44 (2022), [2111.07498 \[physics\]](#).
 - [32] C. Xia, J. Zhang, E. Kerrigan, and G. Rigas, Active flow control for bluff body drag reduction using reinforcement learning with partial measurements, *Journal of Fluid Mechanics* **981**, A17 (2024).
 - [33] P. Suárez, F. Álcantara-Ávila, A. Miró, J. Rabault, B. Font, O. Lehmkuhl, and R. Vinuesa, Active flow control for drag reduction through multi-agent reinforcement learning on a turbulent cylinder at $Re_D=3900$ (2024), [arXiv:2405.17655 \[physics\]](#).

- [34] R. Paris, S. Beneddine, and J. Dandois, Robust flow control and optimal sensor placement using deep reinforcement learning, *Journal of Fluid Mechanics* **913**, A25 (2021).
- [35] J. Rabault and A. Kuhnle, Accelerating deep reinforcement learning strategies of flow control through a multi-environment approach, *Physics of Fluids* **31**, 094105 (2019).
- [36] J. Wang and H. Xu, Optimal parallelization strategies for active flow control in deep reinforcement learning-based computational fluid dynamics, *Physics of Fluids* **36**, 043623 (2024).
- [37] Q. Wang, L. Yan, G. Hu, C. Li, Y. Xiao, H. Xiong, J. Rabault, and B. R. Noack, DRLinFluids: An open-source Python platform of coupling deep reinforcement learning and OpenFOAM, *Physics of Fluids* **34**, 081801 (2022).
- [38] H. Zhu, W. Hao, C. Li, Q. Ding, and B. Wu, Application of flow control strategy of blowing, synthetic and plasma jet actuators in vertical axis wind turbines, *Aerospace Science and Technology* **88**, 468 (2019).
- [39] H. Zong, M. Chiatto, M. Kotsonis, and L. De Luca, Plasma synthetic jet actuators for active flow control, *Actuators* **7**, 10.3390/act7040077 (2018).
- [40] J. C. Lin, Review of research on low-profile vortex generators to control boundary-layer separation, *Progress in Aerospace Sciences* **38**, 389 (2002).
- [41] A. Qayoum, V. Gupta, P. Panigrahi, and K. Muralidhar, Perturbation of a laminar boundary layer by a synthetic jet for heat transfer enhancement, *International Journal of Heat and Mass Transfer* **53**, 5035 (2010).
- [42] H. H. Ho, A. Shirinzad, E. E. Essel, and P. E. Sullivan, Synthetic jet actuators for active flow control: A review, Preprints 10.20944/preprints202410.1798.v1 (2024).
- [43] W.-L. Chen, Y. Huang, C. Chen, H. Yu, and D. Gao, Review of active control of circular cylinder flow, *Ocean Engineering* **258**, 111840 (2022).
- [44] M. Girfoglio, C. S. Greco, M. Chiatto, and L. de Luca, Modelling of efficiency of synthetic jet actuators, *Sensors and Actuators A: Physical* **233**, 512 (2015).
- [45] R. Saidur, N. Rahim, and M. Hasanuzzaman, A review on compressed-air energy use and energy savings, *Renewable and Sustainable Energy Reviews* **14**, 1135 (2010).
- [46] N. Zuckerman and N. Lior, Jet impingement heat transfer: Physics, correlations, and numerical modeling (Elsevier, 2006) pp. 565–631.
- [47] W. Chen, Q. Wang, L. Yan, G. Hu, and B. R. Noack, Deep reinforcement learning-based active flow control of vortex-induced vibration of a square cylinder, *Physics of Fluids* **35**, 053610 (2023).
- [48] L. Yan, Y. Li, G. Hu, W.-I. Chen, W. Zhong, and B. R. Noack, Stabilizing the square cylinder wake using deep reinforcement learning for different jet locations, *Physics of Fluids* **35**, 115104 (2023).
- [49] J. Wang and H. Xu, Effect of synthetic jets actuator parameters on deep reinforcement learning-based flow control performance in a square cylinder, *Physics of Fluids* **36**, 084113 (2024).
- [50] L. Yan, Y. Li, B. Liu, and G. Hu, Aerodynamic force reduction of rectangular cylinder using deep reinforcement learning-controlled multiple jets, *Physics of Fluids* **36**, 025169 (2024).
- [51] T. Suzuki, Effects of a synthetic jet acting on a separated flow over a hump, *Journal of Fluid Mechanics* **547**, 331 (2006).
- [52] R. Ma, C. Gao, K. Ren, H. Yuan, and W. Zhang, Suppression of oscillatory fluid forces in cylinder wake: Optimal jet control position designed through resolvent analysis, *Physics of Fluids* **36**, 073622 (2024).
- [53] Y. Mao, S. Zhong, and H. Yin, Active flow control using deep reinforcement learning with time delays in markov decision process and autoregressive policy, *Physics of Fluids* **34**, 053602 (2022).
- [54] X.-J. He, Y.-Z. Wang, Y. Hua, Z.-H. Chen, Y.-B. Li, and W.-T. Wu, Policy transfer of reinforcement learning-based flow control: From two- to three-dimensional environment, *Physics of Fluids* **35**, 055116 (2023).
- [55] T. Sarpkaya, Vortex-induced oscillations: A selective review, *Journal of Applied Mechanics* **46**, 241 (1979).
- [56] H. Jasak, A. Jemcov, Z. Tukovic, *et al.*, Openfoam: A c++ library for complex physics simulations, in *International Workshop on Coupled Methods in Numerical Dynamics*, Vol. 1000 (2007) pp. 1–20.
- [57] R. I. Issa, Solution of the implicitly discretised fluid flow equations by operator-splitting, *Journal of Computational Physics* **62**, 40 (1986).
- [58] D. Jang, R. Jetli, and S. Acharya, Comparison of the piso, simpler, and simplec algorithms for the treatment of the pressure-velocity coupling in steady flow problems, *Numerical Heat Transfer* **10**, 209 (1986).
- [59] M. Schäfer, S. Turek, F. Durst, E. Krause, and R. Rannacher, Benchmark computations of laminar flow around a cylinder, in *Flow Simulation with High-Performance Computers II*, Notes on Numerical Fluid Mechanics (NNFM), Vol. 48, edited by E. H. Hirschel (Vieweg+Teubner Verlag, 1996) pp. 547–566.
- [60] Y. LeCun, Y. Bengio, and G. Hinton, Deep learning, *Nature* **521**, 436 (2015).
- [61] S. R. Granter, A. H. Beck, and D. J. Papke, Alphago, deep learning, and the future of the human microscopist, *Arch Pathol Lab Med* **141**, 619 (2017).
- [62] H. Wang, N. Liu, Y. Zhang, *et al.*, Deep reinforcement learning: a survey, *Frontiers of Information Technology & Electronic Engineering* **21**, 1726 (2020).
- [63] M. L. Puterman, Chapter 8 markov decision processes, in *Stochastic Models*, Handbooks in Operations Research and Management Science, Vol. 2 (Elsevier, 1990) pp. 331–434.
- [64] E. Altman, *Constrained Markov Decision Processes*, 1st ed. (Routledge, 1999).
- [65] V. Mnih, K. Kavukcuoglu, D. Silver, *et al.*, Human-level control through deep reinforcement learning, *Nature* **518**, 529 (2015).
- [66] L. Kaiser, M. Babaeizadeh, P. Milos, B. Osinski, R. H. Campbell, K. Czechowski, D. Erhan, C. Finn, P. Kozakowski, S. Levine, A. Mohiuddin, R. Sepassi, G. Tucker, and H. Michalewski, *Model-based reinforcement learning for atari* (2024), arXiv:1903.00374 [cs.LG].
- [67] D. Silver, G. Lever, N. Heess, T. Degris, D. Wierstra, and M. Riedmiller, Deterministic policy gradient algorithms, in *Proceedings of the 31st International Conference on Machine Learning*, Proceedings of Machine Learning Research, Vol. 32, edited by E. P. Xing and T. Jebara (PMLR, Beijing, China, 2014) pp. 387–395.

- [68] J. Schulman, S. Levine, P. Abbeel, M. Jordan, and P. Moritz, Trust region policy optimization, in *Proceedings of the 32nd International Conference on Machine Learning*, Proceedings of Machine Learning Research, Vol. 37, edited by F. Bach and D. Blei (PMLR, Lille, France, 2015) pp. 1889–1897.
- [69] C. Szepesvári and M. L. Littman, A unified analysis of value-function-based reinforcement-learning algorithms, *Neural Computation* **11**, 2017 (1999).
- [70] P. Henderson, R. Islam, P. Bachman, J. Pineau, D. Precup, and D. Meger, Deep reinforcement learning that matters, in *Proceedings of the AAAI Conference on Artificial Intelligence*, Vol. 32 (2018).
- [71] D. Fan, L. Yang, Z. Wang, M. S. Triantafyllou, and G. E. Karniadakis, Reinforcement learning for bluff body active flow control in experiments and simulations, *Proceedings of the National Academy of Sciences* **117**, 26091 (2020).
- [72] A. Glezer and M. Amitay, Synthetic jets, *Annual Review of Fluid Mechanics* **34**, 503 (2002).
- [73] B. L. Smith and A. Glezer, The formation and evolution of synthetic jets, *Physics of Fluids* **10**, 2281 (1998).
- [74] M. Amitay, A. Honohan, M. Trautman, and A. Glezer, Modification of the aerodynamic characteristics of bluff bodies using fluidic actuators, in *28th Fluid Dynamics Conference* (AIAA, 1997) p. 2004.